Acta Mech 230, 541–567 (2019)
https://doi.org/10.1007/s00707-018-2346-5

ORIGINAL PAPER

**Elhadji I. Thiam · Enrica Masi · Eric Climent ·
Olivier Simonin · Stéphane Vincent**

Particle-resolved numerical simulations of the gas–solid heat transfer in arrays of random motionless particles

Received: 23 July 2018 / Revised: 20 November 2018 / Published online: 4 February 2019

Abstract Particle-resolved direct numerical simulations of non-isothermal gas–solid flows have been performed and analyzed from microscopic to macroscopic scales. The numerical configuration consists in an assembly of random motionless spherical particles exchanging heat with the surrounding moving fluid throughout the solid surface. Numerical simulations have been carried out using a Lagrangian VOF approach based on fictitious domain framework and penalty methods. The entire numerical approach (numerical solution and post-processing) has first been validated on a single particle through academic test cases of heat transfer by pure diffusion and by forced convection for which analytical solution or empirical correlations are available from the literature. Then, it has been used for simulating gas–solid heat exchanges in dense regimes, fully resolving fluid velocity and temperature evolving within random arrays of fixed particles. Three Reynolds numbers and four solid volume fractions, for unity Prandtl number, have been investigated. Two Nusselt numbers based, respectively, on the fluid temperature and on the bulk (cup-mixing) temperature have been computed and analyzed. Numerical results revealed differences between the two Nusselt numbers for a selected operating point. This outcome shows the inadequacy of the Nusselt number based on the bulk temperature to accurately reproduce the heat transfer rate when an Eulerian–Eulerian approach is used. Finally, a connection between the ratio of the two Nusselt numbers and the fluctuating fluid velocity–temperature correlation in the mean flow direction is pointed out. Based on such a Nusselt number ratio, a model is proposed for it.

1 Introduction

This study deals with the analysis and the modeling of the heat transfer in dense particle-laden flows. Such a regime covers a wide spectrum of industrial applications dealing with energy conversion, manufacturing processes, waste recycling, etc. Many of these applications need to recast their processes in order to comply with new energy and climate targets, thus increasing efficiency while reducing gas emissions. Most of them involve reactive flows in which the heat exchanged between the solid and gaseous phases, and between each phase and the wall, plays a crucial role in the entire process. An understanding of the heat transfers in such complex flows, a long-standing issue, is therefore essential to be able to enhance the performances of existing processes and the development of new technologies. Accordingly, gas–solid heat exchanges have been extensively studied over the years. The particle to fluid heat transfer coefficient in dense regimes (typically fixed or fluidized beds) has been evaluated under theoretical and experimental studies. In the experiments, various methods,

E. I. Thiam · E. Masi (✉) · E. Climent · O. Simonin
Institut de Mécanique des Fluides de Toulouse (IMFT), Université de Toulouse, CNRS, Toulouse, France
E-mail: enrica.masi@imft.fr

S. Vincent
Université Paris-Est Marne la Vallée, Laboratoire de Modélisation et Simulation Multi Echelle (MSME),
UMR 8208 Champs-Sur-Marne, France

designs and operating conditions have been used to determine the heat transfer coefficient over a large range of operating points [1]. However, experimental results exhibited a somewhat large disparity to each other which may be attributed to different experimental techniques employed or, as suggested by Gunn [2], to the different interpretations of raw data. The heat transfer coefficient is indeed the result of a model applied to the experimental quantities, and it strongly depends on the assumptions made. For example, it has been shown and extensively discussed that accounting or not for the axial dispersion in the modeling substantially affects the estimation of the Nusselt number at low Reynolds numbers [1,2]. Moreover, experimental investigations cannot provide a local view of the flow behavior and a deep understanding of the related microscopic features. To overcome these limits, numerical simulation may be used. The latter represents indeed a powerful alternative to experimental investigations, as it is a non-intrusive method able to fully access the local quantities of the particulate flows. To allow the numerical simulation to provide trustworthy heat transfer coefficients, a high accuracy of the results has to be ensured. A high level of accuracy is subject to high resolution, which implies very fine meshes and consequently high computational costs. With the development of high-performance computing (HPC), the direct numerical simulation at microscopic scale (that is at a scale comparable to the particle dimensions) is becoming affordable and thus usable for the investigation of heat exchanges in dense suspensions. By the numerical simulation, Reynolds and Prandtl numbers may be easily changed over a range of intermediate values, thus making it possible to provide Nusselt number correlations as a function of the solid volume fraction and the two aforementioned dimensionless groups. High Reynolds and Prandtl numbers are instead difficult to reproduce because of the small boundary layer thickness and therefore the requirement of even more refined grids. In these last years, several studies using the direct numerical simulation (also referred to as fully resolved or particle-resolved DNS) have been carried out in order to investigate the heat transfer in dense regimes, over intermediate Reynolds and Prandtl numbers and solid concentration up to 50%. These studies employed different numerical strategies for solving the flow interacting with the solid bodies. For example, an immersed boundary method (IBM) for non-isothermal particulate flows was used by Feng and Michaelides [3], Deen et al. [4] and Feng and Musong [5]. Tavassoli et al. [6] extended the approach originally proposed by Uhlmann [7] to account for the heat transport in order to study the heat transfer in particulate flows. These authors reported numerically assessed Nusselt numbers in a random array of fixed spheres in which the fluid flows from an inlet boundary toward an outlet boundary exchanging heat with the solid phase. They provided comparisons with the well-known Gunn correlation [2] and pointed out deviations increasing with the solid volume fractions, considered consistent with the accuracy of such a correlation. Deen et al. [8] reviewed the DNS methods and on the basis of available data refit the Gunn correlation and thus provided a new correlation. The particle-resolved uncontaminated-fluid reconcilable immersed boundary method (PUReIBM) was extended and used in non-isothermal conditions by Tenneti et al. [9] to perform direct numerical simulations of gas–solid heat exchanges within an assembly of random spheres, by using a fully periodic configuration based on a thermal similarity boundary condition for the temperature. Sun et al. [10] suggested a new correlation for the Nusselt number as well as a correction factor to be used in the frame of an Eulerian–Eulerian formulation. Kruggel-Eemden et al. [11] used a lattice Boltzmann method (LBM) to investigate gas-particle heat transfers. Periodic boundary conditions for the flow together with constant and adiabatic conditions at the streamwise boundaries for the temperature were used to simulate heat exchanged in the assembly of random particles. Including the axial dispersion, by using the axial dispersion coefficient proposed by Wakao [1], they obtained Nusselt numbers in good agreement with the correlation proposed by Tavassoli et al. [12]. A new method combining immersed boundary and fictitious domain (referred to as HFD-IB) was recently developed and used to investigate the heat transfer in bi-dispersed regimes by Municchi and Radl [13]. Focusing on the Euler–Lagrange approaches for particulate flows, these authors proposed a closure for the particle Nusselt number as a function of the particle drag force. Alternative methods are also emerging–see, for example, the PHYSALIS method extended to non-isothermal particulate flows by Wang et al. [14]. In the present work, a Lagrangian VOF approach using fictitious domains and penalty methods [15] is used to perform particle-resolved numerical simulations of gas–solid heat transfers. In Sect. 2, such an approach is briefly recalled. A preliminary study devoted to validate the entire methodology (including post-processing strategies) is described in Sect. 3. Direct numerical simulations of gas–solid heat exchanges in arrays of random motionless particles are finally presented in Sect. 4. In the latter, numerical results on two Nusselt numbers based, respectively, on the fluid temperature and on the bulk (cup-mixing) temperature are presented and discussed. Finally, a connection between the ratio of such Nusselt numbers and the fluctuating fluid velocity–temperature term appearing in the energy conservation equation is pointed out. On the basis of this Nusselt number ratio, a model is proposed for it.

2 Numerical modeling

2.1 Governing equations and solution methods

A Lagrangian VOF approach using fictitious domains and penalty methods is used in the present work. It is based on an Eulerian formulation of the Navier–Stokes equations discretized on a fixed structured grid. This approach was initiated by Ritz and Caltagirone [16] for handling particulate flows. To model the behavior of fluid and solid phases, the one-fluid model of Kataoka [17], initially devoted to deformable interfaces and fluid/fluid two-phase flows, was extended to flows interacting with moving finite-size particles by Ritz and Caltagirone [16]. These authors considered the solid particle phase as a continuous phase with high viscosity, requiring a treatment of discontinuities especially for density and viscosity at the interface. With an arithmetic average for the density and a harmonic average for the viscosity at the fluid–solid interfaces, the Stokes flow around a circular cylinder and two-dimensional sedimentation of particles were simulated [16]. This methodology has undergone several improvements, and now, its originality comes from the reformulation of the stress tensor $\left[\mu\left(\nabla\mathbf{u}+(\nabla^T\mathbf{u})\right)\right]$ as proposed by Caltagirone and Vincent [18]. It consists of a decomposition of the stress tensor for Newtonian fluids in order to distinguish the contributions of tearing, shearing and rotation. With the help of a phase function C ($=0$ in fluid medium and $=1$ in solid medium), which describes the solid phase shape evolution through an advection equation (Eq. (2)), classical Navier–Stokes equations are solved for both phases, taking into account the phase behavior:

$$\begin{aligned} &\nabla\cdot\mathbf{u}=0,\\ &\rho\left(\frac{\partial\mathbf{u}}{\partial t}+(\mathbf{u}\cdot\nabla)\mathbf{u}\right)=-\nabla p+\nabla\cdot\left[\mu\left(\nabla\mathbf{u}+(\nabla^T\mathbf{u})\right)\right]+\rho\mathbf{g}+\mathbf{F}_{si}. \end{aligned} \tag{1}$$

In the above system, $\mathbf{u}=(\vec{u},\vec{v},\vec{w})$ and $\mathbf{g}$ are, respectively, the velocity and the gravity vectors, p is the pressure field, ρ and μ are the density and the dynamic viscosity and $\mathbf{F}_{si}$ is the force ensuring coupling between the phases. The spatial and temporal evolution of the phase function then writes:

$$\frac{\partial C}{\partial t}+\mathbf{u}\cdot\nabla C=0. \tag{2}$$

Equation (2) is solved in a Lagrangian manner. The shape of the particles is tracked by a Lagrangian mesh made of triangles in 3D. For spherical particles as in the present work, the advection of the solid phase is satisfied with the Lagrangian tracking of the barycenter of the sphere, using a Runge–Kutta method of second order. The Eulerian phase function is finally obtained at each time step by projecting the Lagrangian meshes of all particles on the Eulerian grid with a kind of Monte Carlo approach. All these procedures are detailed [15]. According to the penalty method acting on the viscosity, no tearing, no shearing and constant rotation could be imposed, for example, to the solid phase. By this approach, the divergence of the viscous stress tensor is indeed written using the decomposition

$$\nabla\cdot\left[\mu\left(\nabla\mathbf{u}+(\nabla^T\mathbf{u})\right)\right]=\nabla\cdot\left[\kappa\boldsymbol{\Lambda}(\mathbf{u})\right]+\nabla\cdot\left[\zeta\boldsymbol{\Theta}(\mathbf{u})\right]-\nabla\cdot\left[\eta\boldsymbol{\Gamma}(\mathbf{u})\right], \tag{3}$$

which makes easier the implementation of a penalty method by imposing separate viscosity coefficients such as the tearing viscosity, κ, the shearing viscosity, ζ, and the rotation viscosity, η, appearing in Eq. (3). The implicit tensorial penalty method (ITPM) for solid behavior and incompressibility constraint is a new evolution, of second-order convergence in space, of the viscous penalty method. Details about this method may be found in Vincent et al. [15]. It is implemented together with an augmented Lagrangian method first proposed by Fortin and Glowinski [19]. Before explaining the specificity of ITPM, we recall the time discretization employed for solving the Eulerian system (1). The temporal derivatives are approximated with implicit finite volume schemes which does not require a stability condition; either Euler or Gear schemes are used depending on the complexity of the problem. A second-order centered scheme is employed to approximate the spatial derivatives. Time derivatives may be written as

$$\frac{\partial\mathbf{u}}{\partial t}\simeq\frac{f(\mathbf{u}^{n+1},\mathbf{u}^{n},\mathbf{u}^{n-1})}{\Delta t},\quad \text{with } \Delta t \text{ the time step,} \tag{4}$$

according to the following schemes:

- Euler: $f(\mathbf{u}^{n+1}, \mathbf{u}^n, \mathbf{u}^{n-1}) = \mathbf{u}^{n+1} - \mathbf{u}^n$,
- Gear: $f(\mathbf{u}^{n+1}, \mathbf{u}^n, \mathbf{u}^{n-1}) = \frac{3}{2}\mathbf{u}^{n+1} - 2\mathbf{u}^n + \frac{1}{2}\mathbf{u}^{n-1}$.

If the Gear scheme is used, the inertial term is linearized by an Adams–Bashforth scheme as follows: $\mathbf{u}^{n+1} \cdot \nabla \mathbf{u}^{n+1} \approx (2\mathbf{u}^n - \mathbf{u}^{n-1}) \cdot \nabla \mathbf{u}^{n+1}$. The augmented Lagrangian method is used to satisfy the incompressibility constraint through a velocity–pressure $(\mathbf{u},\ p)$ coupling, by solving a minimization problem. The approximation of the solution by an Uzawa-like scheme reads:

$$\begin{cases} \text{while } \|\nabla \cdot \mathbf{u}^{n+1,k}\| > \epsilon_1 \\ \rho \left(\frac{f(\mathbf{u}^{n+1}, \mathbf{u}^n, \mathbf{u}^{n-1})}{\Delta t} + ((\mathbf{u}^{n+1,k-1} \cdot \nabla)\mathbf{u}^{n+1,k} \right) - \nabla(r \nabla \cdot \mathbf{u}^{n+1,k}) = -\nabla p^{n,k-1} + \rho \mathbf{g} \\ \qquad\qquad + \nabla \cdot \left[\mu \left(\nabla \mathbf{u}^{n+1,k} + (\nabla^T \mathbf{u}^{n+1,k}) \right) \right] + F_{si}^{n+1,k}, \\ p^{n+1,k} = p^{n,k-1} - r \nabla \cdot \mathbf{u}^{n+1,k}. \end{cases} \tag{5}$$

In the above system, k is the iterative index for the Uzawa optimization algorithm and n the physical time iterative index. The significant parameter in Eq. (5) is the augmented Lagrangian parameter r. In the standard form of the algorithm, r is constant; improvements proposed in [20] used instead a spatial and time parameter $r(x, y, z, t)$ linked to a fixed initial a priori constant value to get a satisfactory solution. Further improvements by Vincent et al. [21] proved that an algebraic parameter r is suitable to fully carry out incompressibility and solid constraints in an optimal way. This algebraic parameter is defined according to the discretization matrix containing the viscous penalty contributions. To implement the penalty method for the viscosity, thanks to the viscous stress tensor decomposition (3), and in order to impose no shearing, no tearing and constant rotation for solid particles, a dual grid (points located at the center of the grid cells) is introduced [15]; the latter allows the specification of shearing and rotation viscosities, while the elongation viscosity is defined on the pressure nodes. Linked to the previous algebraic parameter, solid constraints are ensured at the same time as incompressibility with second-order convergence in space. Then, physical properties at fluid–solid interfaces are defined by using a harmonic average for the viscosities and an arithmetic average for the density. The particle interaction force $\mathbf{F}_{si}$ accounting for particle–particle and particle–wall collisions was implemented and validated by Brändle de Motta et al. [22]. Details about particle tracking and four-way coupling may be found elsewhere [15].

When the particle velocities are not a priori known, ITPM makes it possible to ensure both incompressibility and solid constraints, while, for fixed particles, a simpler penalty method may be employed. The latter, referred to as Darcy penalty method (DPM) [23], is an approach typically used in porous media in order to solve the Navier–Stokes equations accounting for the interactions with a solid object. It consists in considering an additional term in the momentum equation based on a local permeability parameter:

$$\rho \left(\frac{\partial \mathbf{u}}{\partial t} + \mathbf{u} \cdot \nabla \mathbf{u} \right) + \frac{\mu}{K} \mathbf{u} = \nabla \cdot \left[\mu \left(\nabla \mathbf{u} + \nabla^T \mathbf{u} \right) \right] - \nabla p + \rho \mathbf{g}. \tag{6}$$

The permeability K tends to $+\infty$ in the fluid medium and to zero in the solid medium. This method is employed to impose a zero velocity inside the solid. Similarly, a constant temperature can be imposed to the solid. In the energy conservation equation,

$$\rho C_{\mathrm{p}} \left(\frac{\partial T}{\partial t} + \mathbf{u} \cdot \nabla T \right) + \beta (T - T_{\mathrm{s}}) = \nabla \cdot [k_{\mathrm{f}} \nabla T], \tag{7}$$

where T is the phase temperature (with T_{s} the solid one). C_{p} is the mass heat capacity and k_{f} is the thermal conductivity; their respective values are set equal for both the phases in this work. The supplementary term $\beta(T - T_{\mathrm{s}})$ is only active in those zones in which the phase function is equal to unity ($C = 1$) and $\beta \to +\infty$. In the fluid domain, $C = 0$ and $\beta = 0$. The finite volume discretization scheme for the energy conservation equation is based on an explicit total variation diminishing (TVD) scheme for the convection terms, while an implicit centered scheme is used for the conductive terms. An implicit Euler time discretization is used for time derivatives. Linear systems resulting from all discretizations (augmented Lagrangian terms, Navier–Stokes equations, energy equation) are treated with a BiCGSTAB II solver and a modified and incomplete LU preconditioner [15].

2.2 Heat transfer rate computation over a sphere

According to the well-known Newton's law of cooling, the heat transfer rate from a body (at constant temperature T_s) immersed in a infinite fluid (at temperature T_f) relies on a heat transfer coefficient h_f which is defined as a proportionality constant:

$$Q_{\mathrm{b}\to\mathrm{f}} = h_\mathrm{f} A \left(T_\mathrm{s} - T_\mathrm{f}\right). \tag{8}$$

Such a coefficient, h_f, may be obtained by the numerical simulations by computing the rate of heat exchanged throughout the body surface A. For a spherical particle ($b = p$) of surface area $A = S_\mathrm{p}$, the heat transfer rate is written according to Fourier's law modeling the heat flux as

$$Q_{\mathrm{p}\to\mathrm{f}} = \iint\limits_{S_\mathrm{p}} -k_\mathrm{f} \nabla T \cdot \mathbf{n} \,\mathrm{d}S, \tag{9}$$

where k_f is the conductivity of the fluid and $\mathbf{n}$ is the unit vector normal to the solid surface and pointing outward. Numerically, the computation of $Q_{\mathrm{p}\to\mathrm{f}}$ needs a discretization of the sphere surface. The fictitious domain framework, using staggered grid, considers a phase function to locate all control volumes occupied by a particle. In practice, a spherical object is defined, i.e., the particle, and then projected on the structured grid which is used to solve the conservation equations. The surface of this object is discretized by Lagrangian triangle elements. All the coordinates of the vertices of the triangles are recalculated in the real space. Based on the knowledge of the Lagrangian surface particle mesh, the phase function is automatically generated by using ray casting procedures [24]. The heat transfer rate computation can then be achieved by a numerical integration as follows:

$$Q^{\mathrm{num}}_{\mathrm{p}\to\mathrm{f}} = \sum_{\mathrm{b}=1}^{N_\mathrm{b}} -k_\mathrm{f} \nabla T (x_\mathrm{b}, y_\mathrm{b}, z_\mathrm{b}) \cdot \mathbf{n}_\triangledown S_\triangledown, \tag{10}$$

where N_b is the number of triangle elements over the sphere surface. The calculation algorithm consists of four steps. Noting the coordinates as

- $(x_\mathrm{p}, y_\mathrm{p}, z_\mathrm{p})$: the cell centers of the structured Eulerian mesh (pressure nodes),
- $(x_\mathrm{v}, y_\mathrm{v}, z_\mathrm{v})$: the staggered coordinates of the cell faces of the structured Eulerian mesh (velocity nodes),
- $(x_\mathrm{b}, y_\mathrm{b}, z_\mathrm{b})$: the coordinates of the barycenter of each triangle element on the particle surface,

and defining $\mathbf{n}_\triangledown$ and $S_\triangledown$ as, respectively, the normal vector and the surface of each triangle, the algorithm consists in:

1. computing the temperature gradient on the staggered Eulerian grid nodes belonging to the fluid, and interpolating the gradient components from the staggered Eulerian fluid nodes to the pressure fluid nodes
   - $\nabla T_{x_\mathrm{v}} = \frac{T_{i+1,j,k} - T_{i-1,j,k}}{2\Delta x_\mathrm{p}}$, $\nabla T_{x_\mathrm{p}} = \frac{\nabla T_{x\mathrm{v}_{i+1,j,k}} + \nabla T_{x\mathrm{v}_{i-1,j,k}}}{2}$,
   - $\nabla T_{y_\mathrm{v}} = \frac{T_{i,j+1,k} - T_{i,j-1,k}}{2\Delta y_\mathrm{p}}$, $\nabla T_{y_\mathrm{p}} = \frac{\nabla T_{y\mathrm{v}_{i,j+1,k}} + \nabla T_{y\mathrm{v}_{i,j-1,k}}}{2}$,
   - $\nabla T_{z_\mathrm{v}} = \frac{T_{i,j,k+1} - T_{i,j,k-1}}{2\Delta z_\mathrm{p}}$, $\nabla T_{z_\mathrm{p}} = \frac{\nabla T_{z\mathrm{v}_{i,j,k+1}} + \nabla T_{z\mathrm{v}_{i,j,k-1}}}{2}$;
2. computing $\mathbf{n}_\triangledown$ and $S_\triangledown$
   - $\vec{n}_\triangledown = \frac{\vec{U}_{t_1} \wedge \vec{U}_{t_2}}{\|\vec{U}_{t_1} \wedge \vec{U}_{t_2}\|}$, $S_\triangledown = \frac{1}{2} \left\| \vec{U}_{t_1} \wedge \vec{U}_{t_2} \right\|$

   with $\vec{U}_{t_{1,2}}$ the tangent vectors to triangle surface;
3. approximating $\nabla T (x_\mathrm{b}, y_\mathrm{b}, z_\mathrm{b})$ by
   - tracking of a fluid grid cell containing the barycenter of a given particle surface element;
   - Taylor extrapolating $\nabla T (x_\mathrm{b}, y_\mathrm{b}, z_\mathrm{b})$ from neighboring pressure fluid nodes. A fourth-order scheme is used for the approximation of the first derivative in Taylor's extrapolation equation:

$$f(x) = f(x_0) + (f'(x))(x - x_0) + \mathcal{O}(h).$$

In the implementation of this method, the tracking of a fluid grid cell containing the barycenter of a triangle element represents the only difficult point when more than one particle is considered in the domain. Also, the number of grid points to consider in the approximation of the first derivative in Taylor's extrapolation scheme depends on the thickness of the thermal boundary layer.

3 Heat transfer on isolated particle

3.1 Conduction

The first validation test case concerns the unsteady heat diffusion from a spherical particle in a quiescent infinite fluid. A sphere of diameter $d_\mathrm{p} = 2R$ is immersed at the center of a cubic domain of size $8d_\mathrm{p}$. The dimensionless temperature of the fluid is initially set as $T_\mathrm{f} = 0$. A constant dimensionless temperature, $T_\mathrm{s} = 1$, is instead imposed as a boundary condition on the sphere surface, at all times, using the penalty method for the energy equation described previously. Periodic boundary conditions are selected for the outer bounds of the computational domain. The latter is large enough to be considered as infinite, while the thermal diffusion is limited to the vicinity of the sphere (preventing interactions with the boundaries of the domain). Several simulations are performed by varying the mesh size, according to the dimensionless parameter $N_\mathrm{d} = d_\mathrm{p}/\Delta$ where $\Delta = \mathrm{d}x = \mathrm{d}y = \mathrm{d}z$. A visualization of the fluid temperature on a plane taken in the middle of the cube is shown in Fig. 1. The temporal evolution of the temperature profile in the vicinity of the sphere is given by

$$\frac{T_\mathrm{a}(r,t) - T_\mathrm{f}}{(T_\mathrm{s} - T_\mathrm{f})} = \frac{R}{r}\left(1 - \mathrm{erf}\left(\frac{r-R}{\sqrt{4\alpha t}}\right)\right), \ r \geq R, \tag{11}$$

where the thermal diffusivity is defined as $\alpha = k_\mathrm{f}/(\rho_\mathrm{f} C_\mathrm{p})$, where ρ_f is the fluid density. The dimensionless Nusselt number modeling the heat transferred from the particle to the fluid is then defined as follows:

$$\mathrm{Nu} = \frac{h_\mathrm{f} d_\mathrm{p}}{k_\mathrm{f}}. \tag{12}$$

The analytic solution of the Nusselt number can be obtained from Eq. (11), which gives

$$\frac{h_\mathrm{f}}{k_\mathrm{f}} = \frac{-\left.\frac{\partial T_\mathrm{a}(r,t)}{\partial r}\right|_{r=R}}{T_\mathrm{s} - T_\mathrm{f}}, \tag{13}$$

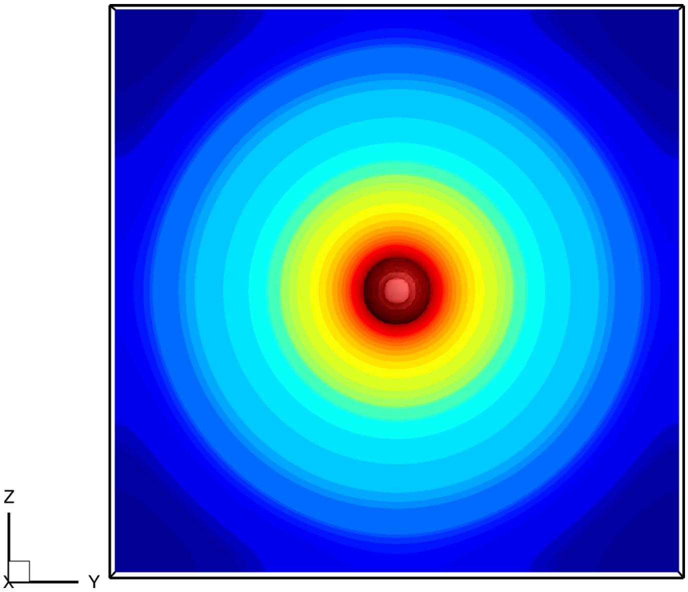

Fig. 1 Temperature field on a slice in the middle of the computational domain

Table 1 Relative error on the temperature near the sphere

Grid size	N_d	$\max(\langle Er_T(r,t)\rangle^t)$
80 × 80 × 80	10	$\sim 22\%$
160 × 160 × 160	20	$\sim 13\%$
240 × 240 × 240	30	$\sim 9\%$
320 × 320 × 320	40	$\sim 6.5\%$
400 × 400 × 400	50	$\sim 2.23\%$
480 × 480 × 480	60	$\sim 0.57\%$
640 × 640 × 640	80	$\sim 0.4\%$

Table 2 Mean relative error $\langle Er_{\mathrm{Nu}}(t)\rangle^t$ depending on grid size and number of elements

N_d	N_b			
	320	4500	18,000	
10	19.41	20.64	20.57	Error (%)
	1.02	14.32	57.29	$N_\mathrm{b}/(\pi N_\mathrm{d}^2)$
20	9.17	7.89	7.93	Error (%)
	0.25	3.58	14.32	$N_\mathrm{b}/(\pi N_\mathrm{d}^2)$
30	7.60	5.19	5.08	Error (%)
	0.11	1.59	6.37	$N_\mathrm{b}/(\pi N_\mathrm{d}^2)$

and finally

$$\mathrm{Nu}(t) = 2 + \frac{2R}{\sqrt{\pi\alpha t}}. \tag{14}$$

This validation aims at verifying the ability of the entire approach to accurately predict the temperature field near the sphere. The relative error between the temperature obtained by the numerical simulation, T_{sim}, and the analytic solution (11) is computed at all nodes of the computational domain as

$$Er_T(r,t) = \frac{|T_{\mathrm{sim}}(r,t) - T_\mathrm{a}(r,t)|}{T_\mathrm{a}(r,t)}. \tag{15}$$

For different grid sizes, N_d spanning from 10 to 80, the maximum of the mean relative error $\langle Er_T(r,t)\rangle^t$ is computed and the results are reported in Table 1. (Results are time-averaged in the interval $t^* \in [1.84, 4.51]$ where $t^* = d_\mathrm{p}/\sqrt{\pi\alpha t}$ is a dimensionless time.) Located at the interface between the fluid and the sphere ($r = R$), the maximum error decreases when the mesh is refined, as expected. For grids coarser than $N_\mathrm{d} = 30$, the error is larger than 10%. It is instead sensibly small for the finest grid $N_\mathrm{d} = 80$. A relative error between predicted and analytic Nusselt numbers is also defined:

$$Er_{\mathrm{Nu}}(t) = \frac{|\mathrm{Nu}_{\mathrm{sim}}(t) - Nu(t)|}{\mathrm{Nu}(t)}. \tag{16}$$

First, the effect of the number of elements on the sphere surface is analyzed. Table 2 shows the mean (time-averaged in the interval $t^* \in [2.26, 4.51]$) relative error for three meshes $N_\mathrm{d} = 10,\ 20,\ 30$ and three different triangularizations of the sphere surface. Results show that 4500 elements are enough to obtain a converged Nusselt number on a selected grid, allowing to perform a grid convergence analysis. Such a value is therefore retained in the present study. In Table 2, the ratio between the surface elements (N_b) and the number of grid cells over the particle surface (estimated as πN_d^2) is also reported.[1] Results seem to indicate that numerical simulations become independent of N_b when at least one surface element is present for each cell over the particle surface (i.e., $N_\mathrm{b}/\pi N_\mathrm{d}^2 > 1$). Accordingly to the choice $N_\mathrm{b} = 4500$, the effect of the mesh size on the Nusselt predictions is analyzed. Figure 2 shows the temporal evolution of the analytic and computed Nusselt numbers for $N_\mathrm{d} = 80$. (Vertical lines correspond to the time interval used for assessing the mean error.) The mean relative error as a function of the grid size is also plotted. The error decreases with the mesh refinement, and from $N_\mathrm{d} = 20$, it becomes smaller than 10%. The order of convergence is about 1 up to $N_\mathrm{d} = 40$. Further, as the time advances, the instantaneous error decreases even more (Table 3).

---

[1] The authors thank the anonymous reviewer for the suggestion.

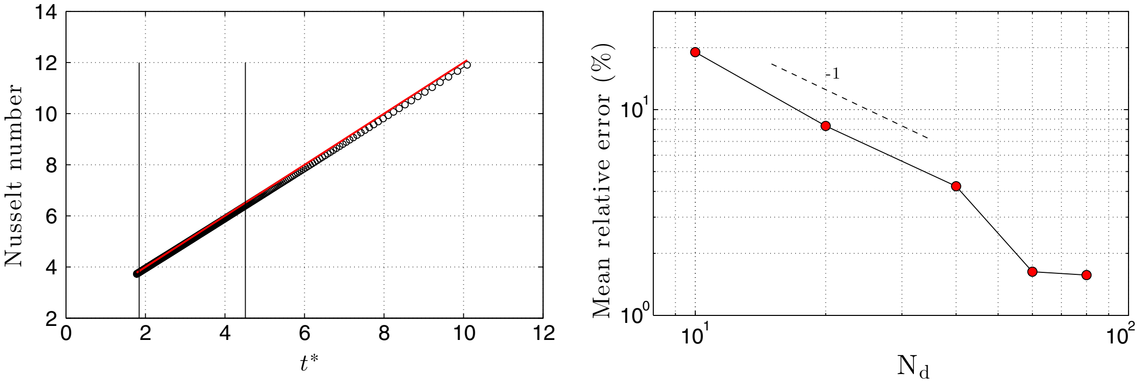

Fig. 2 Analytic (solid line) versus numerical (symbols) Nusselt number for $N_d = 80$ (left). Mean relative error (right)

Table 3 Analytic versus predicted instantaneous Nusselt number for $N_d = 80$

t^*	Nu_{sim}	Nu	$Er_{Nu}(t^*)$
4.51	6.39	6.51	1.84 %
2.61	4.53	4.60	1.52 %
2.02	3.96	4.01	1.25 %

Table 4 Parameters used for the numerical simulation of forced convection around a sphere

Parameter	Value	Unit
Fluid density	1	kg/m^3
Fluid viscosity	1×10^{-5}	Pa.s
Particle diameter	2×10^{-3}	m
Domain size	$7.5d_p \times 4d_p \times 4d_p$	m^3
N_d	$10,\ 20,\ 40,\ 60,\ 80$	–
Boundary conditions		
Inlet	Outlet	Lateral faces
$U_\infty = 0.05, 0.25, 0.5$ m/s	$\partial U/\partial x = 0$	Periodic
$T_\infty = 275$ K	$\partial T/\partial x = 0$	Periodic

3.2 Forced convection

The second validation test case concerns the heat transfer occurring in a fluid at temperature T_∞ flowing at velocity U_∞ over a sphere of diameter d_p whose temperature is fixed to T_s. The Reynolds number ($Re = \rho_f U_\infty d_p/\mu$) is varied by changing the inlet velocity, and the Prandtl number ($Pr = \mu C_p/k_f$) is imposed equal to unity. This corresponds to a case of forced convection around a fixed spherical particle. Using the DPM approach, a no-slip condition at the particle surface is imposed, which implies zero velocity in all grid points standing within the particle volume. The spherical particle is placed at $2d_p$ from the fluid inlet boundary and its temperature is fixed to 320 K. Physical and numerical parameters of the simulations are given in Table 4. For Reynolds numbers 10, 50 and 100, by computing the heat transfer coefficient, we aim at determining the Nusselt number modeling the heat exchanged between the fluid and the particle surface and compare it with the correlations from the literature. A visualization of the temperature field on a plane in the middle of the computational domain is shown in Fig. 3. Before proceeding with the Nusselt number analysis, we first check the total hydrodynamic drag force (F_{p_n}) acting on the sphere. The numerical integration of Eq. (17) is performed in the same way as the heat flux by triangularization of the sphere surface using $N_b = 4500$ elements. The pressure and viscous stresses are extrapolated to the barycenter of triangular elements with a fourth-order Taylor scheme.

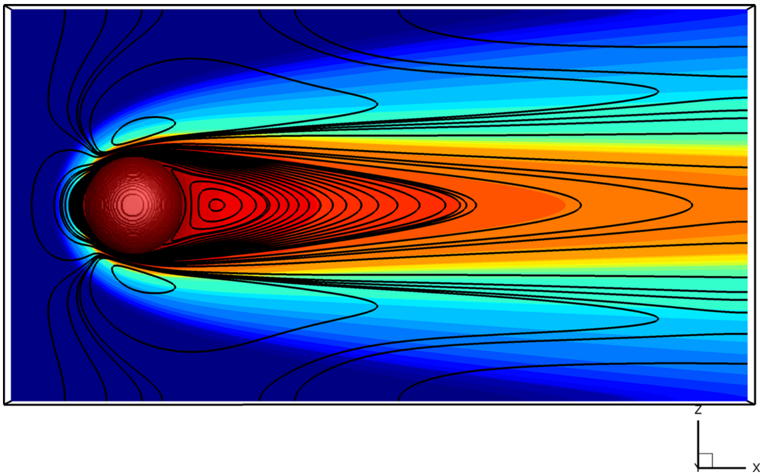

Fig. 3 Temperature spatial distribution with flow streamlines around the hot sphere at $Re = 100$

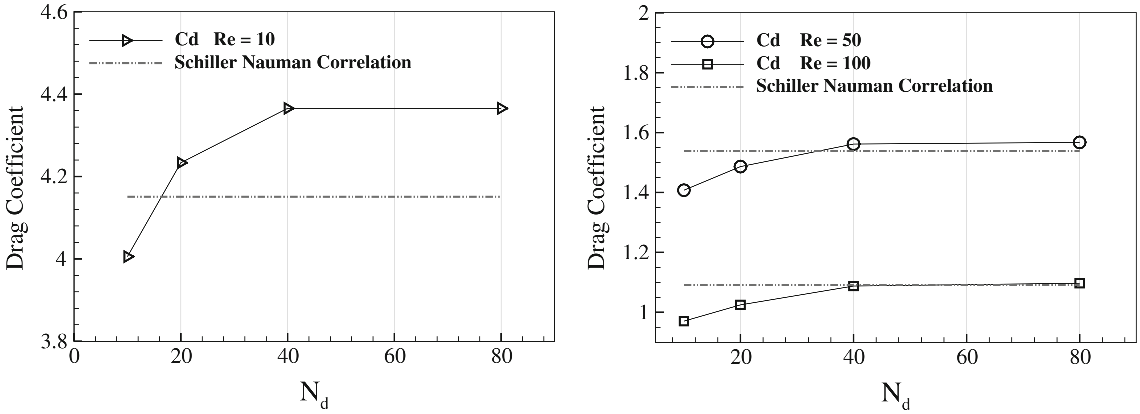

Fig. 4 Drag coefficient for $Re = 10$ ▷ (left) and $Re = 50$ ○ and $Re = 100$ □ (right) compared to Schiller–Naumann's correlation

$$\mathbf{F}_{p_n} = \iint_{S_\mathrm{p}} \left(-p\mathbb{I} + \left[\mu\left(\nabla\mathbf{u} + (\nabla^T\mathbf{u})\right)\right]\right)\cdot\mathbf{n}\,\mathrm{d}S. \tag{17}$$

The drag coefficient [Eq. (18)] is compared to the well-known Schiller–Naumann's correlation (Eq. (19)) for grid sizes $N_\mathrm{d} = 10,\ 20\,40,\ 80$:

$$\mathrm{Cd} = \frac{||\mathbf{F}_{p_n}||}{\frac{\pi}{8}\,d_\mathrm{p}^2\,\rho_\mathrm{f}\,U_\infty^2}, \tag{18}$$

$$\mathrm{Cd} = \frac{24}{Re}\left(1 + 0.15Re^{0.687}\right). \tag{19}$$

In Fig. 4, the convergence is shown for all the Reynolds numbers we tested. A $\sim 5\%$ deviation from the Schiller–Naumann correlation is observed for $Re = 10$, while results agree very well with such a correlation for higher Reynolds number from 40 grid cells per particle diameter. The heat transfer coefficient corresponds to the ratio between the total heat transfer rate and the difference between the solid temperature and the undisturbed fluid temperature multiplied by the total exchanging area:

$$h_\mathrm{f} = \frac{Q_{\mathrm{p}\rightarrow\mathrm{f}}}{(T_\mathrm{s} - T_\infty)(4\pi R^2)}. \tag{20}$$

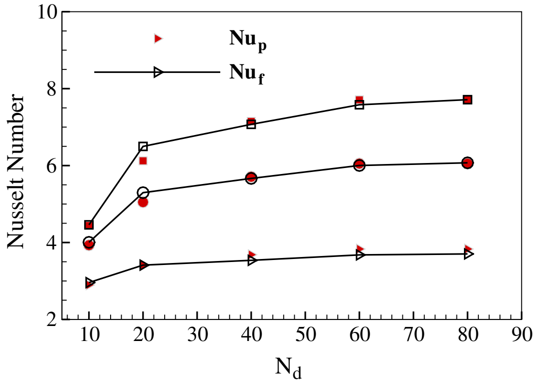

Fig. 5 Comparison of Nusselt numbers $\mathrm{Nu_f}$ and $\mathrm{Nu_p}$ at $Re = 10$ ▷, $Re = 50$ ○, and $Re = 100$ □ as a function of the grid resolution

From the heat transfer coefficient (Eq. (20)), the Nusselt number may be obtained. To compute the heat transfer rate $Q_{\mathrm{p}\to\mathrm{f}}$ from the simulations, two methods are tested. First, $Q_{\mathrm{p}\to\mathrm{f}}$ (referred to as Q_{f}) is estimated from an inlet–outlet integral heat balance as

$$Q_{\mathrm{f}} = \iint_{S_{\mathrm{In}}} \rho_{\mathrm{f}} C_{\mathrm{p}} T \mathbf{u} \cdot \mathbf{n} \, \mathrm{d}S + \iint_{S_{\mathrm{Out}}} \rho_{\mathrm{f}} C_{\mathrm{p}} T \mathbf{u} \cdot \mathbf{n} \, \mathrm{d}S, \tag{21}$$

where S_{In} and S_{Out} are, respectively, the inlet and the outlet cross-sectional areas of the computational domain. This gives $\mathrm{Nu_f} = Q_{\mathrm{f}} d_{\mathrm{p}} / (k_{\mathrm{f}}(T_{\mathrm{s}} - T_{\infty})(4\pi R^2))$. Then, $Q_{\mathrm{p}\to\mathrm{f}}$ (referred to as Q_{p}), is computed by the heat flux integrated over the sphere surface (Eq. (9)) with the algorithm described in Sect. 2.2, leading to defining $\mathrm{Nu_p} = Q_{\mathrm{p}} d_{\mathrm{p}} / (k_{\mathrm{f}}(T_{\mathrm{s}} - T_{\infty})(4\pi R^2))$. By the numerical simulations, we study the sensitivity of both the Nusselt numbers $\mathrm{Nu_f}$ and $\mathrm{Nu_p}$ to the grid size. Results are shown in Fig. 5. Comparison between the two quantities reveals that the two ways of computations are very similar. Results also show that the larger is the Reynolds number the higher should be the grid resolution, as expected. This depends on the thickness of the boundary layer which decreases with the Reynolds number. Grids even more refined should be employed when the Prandtl number increases ($Pr \gg 1$) because of the decrease in the thermal boundary layer thickness. The grid convergence analysis indicates that for $Re = 10$, 20 cells per particle diameter are sufficient to get quite converged values of the Nusselt number, while for $Re = 50$ and $Re = 100$, at least 40 and 60 cells per particle diameter, respectively, are required. In this configuration of forced convection, different correlations of the Nusselt number are reported in the literature. Some of them are listed below:

Frossling [25]

$$\mathrm{Nu} = 2 + 0.552(Pr)^{1/3}(Re)^{1/2}, \; 2 < Re < 800, \; 0.6 < Pr < 2.7 \tag{22}$$

Ranz and Marshall [26]

$$\mathrm{Nu} = 2 + 0.6(Pr)^{1/3}(Re)^{1/2}, \; 2 \le Re \le 10^4, \; 0.6 \le Pr \tag{23}$$

Whitaker [27]

$$\mathrm{Nu} = 2 + (0.4Re^{1/2} + 0.06Re^{2/3})P_{\mathrm{r}}^{2/5}\left(\frac{\mu_{\mathrm{f}}}{\mu_{\mathrm{s}}}\right)^{1/4}, \; 0.71 \le P_r \le 380, \; 3.5 \le Pe \le 7.6 \times 10^4, \; 1 \le \frac{\mu_{\mathrm{f}}}{\mu_{\mathrm{s}}} \le 3.2 \tag{24}$$

Feng and Michealides [28]

$$\mathrm{Nu} = 0.992 + (\mathrm{Pe})^{1/3} + 0.1(Pe)^{1/3}(Re)^{1/3}, \; 0.1 \le Re \le 4000, \; 0.2 \le Pe \le 2000. \tag{25}$$

Recently, Tavassoli et al. [6], by using an IBM approach at Reynolds numbers $\in [20 - 100]$ and $Pr = 1$, obtained Nusselt numbers close to the correlation of Ranz and Marshall [26]. Kruggel-Eemden et al. [11], by a LBM approach ($\mathrm{Re} \in [20 - 100]$), obtained results which agree more with Feng and Michaelides's correlation [28] for $Pr = 0.7$, while for $Pr = 1$ results in between the correlations of Ranz and Marshall [26] and Feng and Michaelides [28] were found. Figure 6 shows the evolution of the Nusselt number computed by our numerical simulations using the finest computational grid and compared to the empirical aforementioned correlations. Our results agree with Feng and Michaelides's correlation [28] as well.

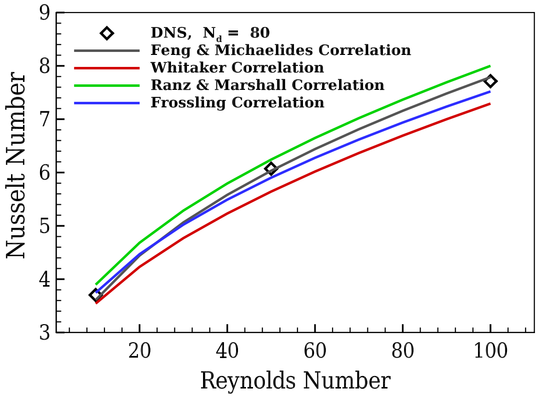

Fig. 6 Nusselt number as a function of Reynolds number obtained by the numerical simulations, using $N_\mathrm{d} = 80$, compared with the correlations from the literature

4 Heat transfer in arrays of random motionless particles

4.1 Computing heat exchanges

We consider a fluid flowing through a static array of heated spherical particles. From the inlet, the fluid reaches the particles, randomly distributed in the domain, with a velocity U_In and a temperature T_In. At the outlet, Neumann conditions are imposed for the fluid velocity and temperature derivatives in the streamwise direction (x). Periodic boundary conditions are instead used in the spanwise directions. Inside the array, the fluid exchanges heat with the particles. The particle temperature is set larger than the fluid temperature, $T_\mathrm{s} > T_\mathrm{In}$, and it is maintained constant during the numerical simulation using the penalization method detailed in Sect. 2 (Eq. (7)). Accordingly, the fluid leaves the domain warmer than when it entered. The method used to compute the solid-to-fluid heat exchanges is presented below.

Let us start with the energy transport equation for the fluid written in a conservative form:

$$\frac{\partial \rho_\mathrm{f} C_\mathrm{p} T}{\partial t} + \nabla \cdot \left(\rho_\mathrm{f} C_\mathrm{p} T \mathbf{u}\right) = \nabla \cdot (k_\mathrm{f} \nabla T). \tag{26}$$

Multiplying Eq. (26) by the fluid phase function $\chi = 1 - C$, and integrating over a volume of control $\mathcal{V}$, makes it possible to obtain a local and instantaneous equation for the fluid, where the heat exchanged with the particulate phase is taken into account at a scale larger than the microscopic scale (that is, at mesoscopic or macroscopic scale, depending on the characteristic length scale of $\mathcal{V}$). Assuming steady conditions, the volume integration of the energy equation (26) leads to writing

$$\iiint\limits_{\mathcal{V}} \chi \nabla \cdot \left(\rho_\mathrm{f} C_\mathrm{p} T \mathbf{u}\right) \,\mathrm{d}\mathcal{V} = \iiint\limits_{\mathcal{V}} \chi \nabla \cdot (k_\mathrm{f} \nabla T) \,\mathrm{d}\mathcal{V}, \tag{27}$$

which, rearranged, gives

$$\iiint\limits_{\mathcal{V}} \nabla \cdot \left(\chi \rho_\mathrm{f} C_\mathrm{p} T \mathbf{u}\right) \,\mathrm{d}\mathcal{V} - \iiint\limits_{\mathcal{V}} \left(\rho_\mathrm{f} C_\mathrm{p} T \mathbf{u}\right) \cdot \nabla \chi \,\mathrm{d}\mathcal{V} = \iiint\limits_{\mathcal{V}} \nabla \cdot (\chi k_\mathrm{f} \nabla T) \,\mathrm{d}\mathcal{V} - \iiint\limits_{\mathcal{V}} k_\mathrm{f} \nabla T \cdot \nabla \chi \,\mathrm{d}\mathcal{V}. \tag{28}$$

The derivative of the fluid phase function verifies the relation $\nabla \chi = -\mathbf{n}_{\sigma_I} \delta_{\sigma_I}$, where $\mathbf{n}_{\sigma_I}$ is the unit normal vector at the fluid–particle interface pointing outward from the fluid region and δ_{σ_I} is the Dirac distribution associated with each interface σ_I [29,30]. According to the interface boundary conditions, without interface mass transfer, $\mathbf{u} \cdot \nabla \chi = 0$ at each σ_I. In Eq. (28), the second term on the left-hand side (l.h.s.) is therefore null everywhere in the domain. The last term on the right-hand side (r.h.s.) represents the heat transfer rate between the solid and the fluid phase and may be written as

$$\mathcal{Q}_{\mathrm{p}\to\mathrm{f}} = -\iiint\limits_{\mathcal{V}} k_\mathrm{f} \nabla T \cdot \nabla \chi \,\mathrm{d}\mathcal{V} = \iint\limits_{\Sigma_I} k_\mathrm{f} \nabla T \cdot \mathbf{n}_{\sigma_I} \,\mathrm{d}S, \tag{29}$$

where $\varSigma_I$ is the whole fluid–solid interface within the selected volume $\mathcal{V}$. If the N_{p} particles are entirely contained into the volume of control $\mathcal{V}$, the heat exchanged between the solid and the fluid may be estimated by integrating over all the particles within $\mathcal{V}$, namely

$$\mathcal{Q}_{\mathrm{p}\to\mathrm{f}} = \sum_{k=1}^{N_{\mathrm{p}}} \mathcal{Q}_{\mathrm{p}}^{(k)}. \tag{30}$$

From Eq. (28), using the divergence theorem, $\mathcal{Q}_{\mathrm{p}\to\mathrm{f}}$ may also be obtained as follows:

$$\mathcal{Q}_{\mathrm{p}\to\mathrm{f}} = \iint\limits_{\varSigma} \chi\rho_{\mathrm{f}} C_{\mathrm{p}} T\mathbf{u}\cdot\mathbf{n}\,\mathrm{d}S - \iint\limits_{\varSigma} \chi k_{\mathrm{f}} \nabla T\cdot\mathbf{n}\,\mathrm{d}S, \tag{31}$$

where $\varSigma$ is the boundary surface of the volume of control $\mathcal{V}$. Equations (30) and (31) are strictly equivalent and should provide equivalent results, unless inaccuracy of numerical approximations. They will be both employed for computing $\mathcal{Q}_{\mathrm{p}\to\mathrm{f}}$. Results will be shown in Sect. 4.3.

4.2 Modeling heat transport and transfer

Fully resolved particle numerical simulations make it possible to estimate the heat exchanged between the solid and the fluid phases. However, this quantity needs to be modeled, at mesoscopic or macroscopic level, when direct numerical simulations are not feasible and fluid and particle equations require closure laws. In this study, we will focus on the macroscopic modeling and investigate the Nusselt number to being used in an Eulerian–Eulerian approach. In order to proceed with the analysis, we introduce a mean (volume-averaged) energy transport equation, on the basis of the previous notations. Defining the mean volume fraction of the fluid within the control volume $\mathcal{V}$ as

$$\phi_{\mathrm{f}} = \frac{1}{\mathcal{V}} \iiint\limits_{\mathcal{V}} \chi\,\mathrm{d}\mathcal{V}, \tag{32}$$

the volume average of the generic quantity, ψ, then writes

$$\phi_{\mathrm{f}}\langle\psi\rangle_{\mathrm{f}} = \frac{1}{\mathcal{V}} \iiint\limits_{\mathcal{V}} \chi\psi\,\mathrm{d}\mathcal{V}. \tag{33}$$

From Eq. (28), assuming that integral and derivative operators commute and assuming constant fluid density, heat capacity and conductivity, the first term on the l.h.s. may be reformulated as follows:

$$\frac{1}{\mathcal{V}} \iiint\limits_{\mathcal{V}} \nabla\cdot\left(\chi\rho_{\mathrm{f}} C_{\mathrm{p}} T\mathbf{u}\right)\,\mathrm{d}\mathcal{V} = \nabla\cdot\left(\phi_{\mathrm{f}}\rho_{\mathrm{f}} C_{\mathrm{p}}\langle T\mathbf{u}\rangle_{\mathrm{f}}\right) = \nabla\cdot\left(\phi_{\mathrm{f}}\rho_{\mathrm{f}} C_{\mathrm{p}}\mathbb{T}_{\mathrm{b}}\cdot\mathbf{U}_{\mathrm{f}}\right), \tag{34}$$

where $\mathbf{U}_{\mathrm{f}} = \langle\mathbf{u}\rangle_{\mathrm{f}}$ is the mean (volume-averaged) fluid velocity and $\mathbb{T}_{\mathrm{b}}$ is a bulk temperature tensor defined as $\mathcal{T}_{\mathrm{b},ij} = (\langle Tu_i\rangle_f U_{f,j})/||\mathbf{U}_{\mathrm{f}}||^2$. In the mean flow direction, when the mean flow is aligned to the mean heat flux, only one component of this tensor prevails. This component corresponds to the well-known bulk (or cup-mixing) temperature, T_{b}, as classically defined in the literature.
The first term on the r.h.s. in Eq. (28) is also rewritten using mean quantities as

$$\frac{1}{\mathcal{V}} \iiint\limits_{\mathcal{V}} \nabla\cdot(\chi k_{\mathrm{f}}\nabla T)\,\mathrm{d}\mathcal{V} = \nabla\cdot\left(\phi_{\mathrm{f}} k_{\mathrm{f}}\langle\nabla T\rangle_f\right) \simeq \nabla\cdot(\phi_{\mathrm{f}} k_{\mathrm{f}}\nabla T_{\mathrm{f}})\,^{2} \tag{35}$$

with $T_{\mathrm{f}} = \langle T\rangle_{\mathrm{f}}$ the mean (volume-averaged) fluid temperature. At the steady state, the local equation modeling the fluid at macroscopic scale takes the form

$$\nabla\cdot\left(\phi_{\mathrm{f}}\rho_{\mathrm{f}} C_{\mathrm{p}}\mathbb{T}_{\mathrm{b}}\cdot\mathbf{U}_{\mathrm{f}}\right) = \nabla\cdot(\phi_{\mathrm{f}} k_{\mathrm{f}}\nabla T_{\mathrm{f}}) + \mathcal{Q}^{*}_{\mathrm{p}\to\mathrm{f}}, \tag{36}$$

---

[2] Generally, $\langle\nabla\psi\rangle_f \neq \nabla\langle\psi\rangle_f$. The corresponding difference is referred to as tortousity in the literature and usually modeled in porous media [29,30].

where $\mathcal{Q}^*_{\mathrm{p}\to\mathrm{f}}$ is the heat transfer rate per unit volume. This formulation makes appear different temperatures which cannot be used in a macroscopic model without any additional assumption. Equation (36) may be rearranged as follows:

$$\nabla \cdot \left(\phi_\mathrm{f} \rho_\mathrm{f} C_\mathrm{p} \mathbf{U}_\mathrm{f}\, T_\mathrm{f}\right) = \nabla \cdot \left(\phi_\mathrm{f} k_\mathrm{f} \nabla T_\mathrm{f}\right) + \mathcal{Q}^*_{\mathrm{p}\to\mathrm{f}} + \nabla \cdot \left(\phi_\mathrm{f} \rho_\mathrm{f} C_\mathrm{p} (T_\mathrm{f} \mathbb{I} - \mathbb{T}_\mathrm{b}) \cdot \mathbf{U}_\mathrm{f}\right). \tag{37}$$

The last term may be written by expressing $\mathcal{T}_{\mathrm{b},ij}$ on the basis of mean and fluctuating quantities as

$$\mathcal{T}_{\mathrm{b},ij} = \langle T u_\mathrm{i} \rangle_\mathrm{f} \frac{U_{\mathrm{f},j}}{||\mathbf{U}_\mathrm{f}||^2} = T_\mathrm{f} \frac{U_{f,i} U_{f,j}}{||\mathbf{U}_\mathrm{f}||^2} + \langle T' u'_i \rangle_\mathrm{f} \frac{U_{f,j}}{||\mathbf{U}_\mathrm{f}||^2}; \tag{38}$$

the generic fluctuation is defined as $\psi' = \psi - < \psi >_\mathrm{f}$ and its average is null over the domain $\mathcal{V}$, by definition. From Eqs. (37), (38) may be formulated as follows:

$$\nabla \cdot \left(\phi_\mathrm{f} \rho_\mathrm{f} C_\mathrm{p} \mathbf{U}_\mathrm{f}\, T_\mathrm{f}\right) = \nabla \cdot \left(\phi_\mathrm{f} k_\mathrm{f} \nabla T_\mathrm{f}\right) + \mathcal{Q}^*_{\mathrm{p}\to\mathrm{f}} - \nabla \cdot \left(\phi_\mathrm{f} \rho_\mathrm{f} C_\mathrm{p} \langle T' \mathbf{u}' \rangle_\mathrm{f}\right). \tag{39}$$

Equation (39) has the form of the energy balance equation commonly used in an Eulerian–Eulerian approach, although it is here obtained by a volume average instead of an ensemble average. Each term in Eq. (39) should be statistically evaluated over a large number of two-phase flow realizations in order to account for the random effect originating from the different particle arrangements. The last term in Eq. (39) represents the energy transport by the velocity–temperature covariance. It intrinsically accounts for all the correlations between fluctuating velocity and temperature in the fluid, irrespective of their nature. In the frame of RANS Eulerian–Eulerian approach, when the fluid is mainly dominated by turbulent effects at large scale with respect to the particle size, this term may be closed using a turbulent thermal diffusivity, derived from a Boussinesq eddy-viscosity assumption, in which the effect of the particles on the fluid is accounted for by using a modified turbulent viscosity [31]. For low Reynolds number and high solid volume fraction, it rather accounts for the correlations induced by the microstructure of the particulate flow and by the particle wake interactions. Such a contribution is modeled in porous media, for example, throughout effective properties (see, for example, the references [32,33]). Instead, it is generally neglected in the Eulerian–Eulerian approaches for fluid–particle flows. Recently, Sun et al. [34] used the fully resolved particle numerical simulation for characterizing this contribution (referred to as pseudo-turbulent heat flux) and proposed a closure for it. Such a closure is a gradient model based on a pseudo-turbulent thermal diffusivity, derived by fitting their fully resolved particle numerical results. In the present work, this contribution is investigated and related to the Nusselt number correlations available from the literature.

In an Eulerian–Eulerian approach, $\mathcal{Q}^*_{\mathrm{p}\to\mathrm{f}}$ is modeled on the basis of a relative (solid-to-fluid) temperature and a heat transfer coefficient as follows:

$$\mathcal{Q}^*_{\mathrm{p}\to\mathrm{f}} = h_\mathrm{f} \mathcal{S}_\mathrm{p} (T_\mathrm{s} - T_\mathrm{f}); \tag{40}$$

T_s represents the temperature of the particulate phase, while T_f is the temperature of the fluid at the same location (both being Eulerian quantities). This modeling cannot account for the undisturbed fluid temperature seen by the particle since only the mean temperature T_f is available at the corresponding Eulerian computational node. In Eq. (40), $\mathcal{S}_\mathrm{p}$ is the total surface of the solid phase per unit volume, which may be written as $6\phi_\mathrm{s}/d_\mathrm{p}$, where $\phi_\mathrm{s} = 1 - \phi_\mathrm{f}$ is the solid volume fraction; h_f is the heat transfer coefficient estimated on the basis of the aforementioned non-dimensional Nusselt number as $h_\mathrm{f} = \mathrm{Nu}_\mathrm{f}\, k_\mathrm{f}/d_\mathrm{p}$. Using the above definitions, Eq. (40) takes the form

$$\mathcal{Q}^*_{\mathrm{p}\to\mathrm{f}} = \frac{6\phi_\mathrm{s} k_\mathrm{f} \mathrm{Nu}_\mathrm{f}}{d_\mathrm{p}^2} (T_\mathrm{s} - T_\mathrm{f}); \tag{41}$$

the latter is closed provided that the Nusselt number is known. Conversely, using the fully resolved particle numerical simulations, a heat transfer coefficient is estimated as

$$h_\mathrm{f} = \frac{\mathcal{Q}^*_{\mathrm{p}\to\mathrm{f}}}{\mathcal{S}_\mathrm{p}(T_\mathrm{s} - T_\mathrm{f})}, \tag{42}$$

and a Nusselt number obtained as

$$\mathrm{Nu}_\mathrm{f} = \frac{h_\mathrm{f}\, d_\mathrm{p}}{k_\mathrm{f}}. \tag{43}$$

However, most of the studies in the literature are modeling the solid-to-fluid heat exchange using the bulk temperature:

$$\mathcal{Q}^*_{\mathrm{p}\to\mathrm{f}} = \frac{6\phi_\mathrm{s} k_\mathrm{f} \mathrm{Nu}_\mathrm{b}}{d_\mathrm{p}^2}(T_\mathrm{s} - T_\mathrm{b}). \tag{44}$$

Such a temperature corresponds to the trace of the tensor $\mathbb{T}_\mathrm{b}$ which reduces to the tensor component $T_\mathrm{b} = \mathcal{T}_{\mathrm{b},\alpha\alpha}$ when the flow mean velocity is aligned to the α direction. The related Nusselt number

$$\mathrm{Nu}_\mathrm{b} = \frac{h_b\, d_\mathrm{p}}{k_\mathrm{f}} \tag{45}$$

is then based on a heat transfer coefficient defined as

$$h_\mathrm{b} = \frac{\mathcal{Q}^*_{\mathrm{p}\to\mathrm{f}}}{\mathcal{S}_\mathrm{p}(T_\mathrm{s} - T_\mathrm{b})}, \tag{46}$$

which is different from that introduced in equation (42). The two definitions (41) and (44) lead to the following relation

$$\mathrm{Nu}_\mathrm{f}(T_\mathrm{s} - T_\mathrm{f}) = \mathrm{Nu}_\mathrm{b}(T_\mathrm{s} - T_\mathrm{b}). \tag{47}$$

In the present work, $T_\mathrm{b} = \mathcal{T}_{\mathrm{b},xx}$ since the x-axis represents the direction of the mean flow (streamwise direction). Equation (47) will be verified by the direct numerical simulation. The difference between the bulk and the mean fluid temperature will be investigated, as well as the two dimensionless Nusselt numbers and their connection with the pseudo-turbulent heat flux.

4.3 Numerical simulations, results and discussions

The computational domain is composed of three zones: an entrance zone, a packed zone and an exit region, as proposed by Tavassoli et al. [6]. Such a configuration allows the simulation to reproduce a fluid flowing through a packed bed of fixed spheres, with uniform inlet velocity and temperature. The particles are randomly distributed in the packed zone distant $2d_\mathrm{p}$ from the entrance and $2d_\mathrm{p}$ from the exit. In the present work, numerical simulations with five different random particle seedings are performed, each one for three Reynolds numbers $(10,\ 50,\ 100)$ and four solid volume fractions $(0.1,\ 0.2,\ 0.3,\ 0.4)$. Numerical simulations use a grid size corresponding to the normalized grid resolution parameter $N_\mathrm{d} = 20$. The latter was indeed found to be a good compromise between accuracy and computational costs in fixed beds. For the solid volume fraction $\phi_\mathrm{s} = 0.1,\ 0.2,\ 0.3$, the number of particles was set to $N_\mathrm{p} = 98,\ 196,\ 294$, respectively, within the same geometrical domain. For the solid fraction $\phi_\mathrm{s} = 0.4$, the packed section was instead reduced in order to obtain fast convergence of the random draw algorithm, and a number of particle $N_\mathrm{p} = 166$ was accordingly used. The Reynolds number, $Re = \rho_\mathrm{f} U_\mathrm{In} d_\mathrm{p}/\mu$, was varied by changing the inlet velocity. The Prandtl number was fixed equal to unity for all the simulations. A summary of the physical and numerical parameters is given in Table 5.

Table 5 Parameters used for simulation of flows through a fixed array of particles

Parameter	Value	Unit
Fluid density ρ_f	1	kg/m^3
Fluid viscosity μ_f	1×10^{-4}	Pa.s
Fluid mass heat capacity C_p	1×10^{3}	J/(Kg K)
Fluid thermal conductivity k_f	1×10^{-1}	W/(m K)
Particle diameter d_p	1×10^{-3}	m
Domain size ($\phi_\mathrm{s} = 0.1, 0.2, 0.3$)	$12d_\mathrm{p} \times 8d_\mathrm{p} \times 8d_\mathrm{p}$	m^3
Domain size ($\phi_\mathrm{s} = 0.4$)	$10d_\mathrm{p} \times 6d_\mathrm{p} \times 6d_\mathrm{p}$	m^3
Grid resolution N_d	20	–
Boundary conditions		
Inlet	Outlet	Lateral faces
$U_\mathrm{In} = 0.1, 0.5, 1$ m/s	$\partial U/\partial x = 0$	Periodic
$T_\mathrm{In} = 275$ K	$\partial T/\partial x = 0$	Periodic

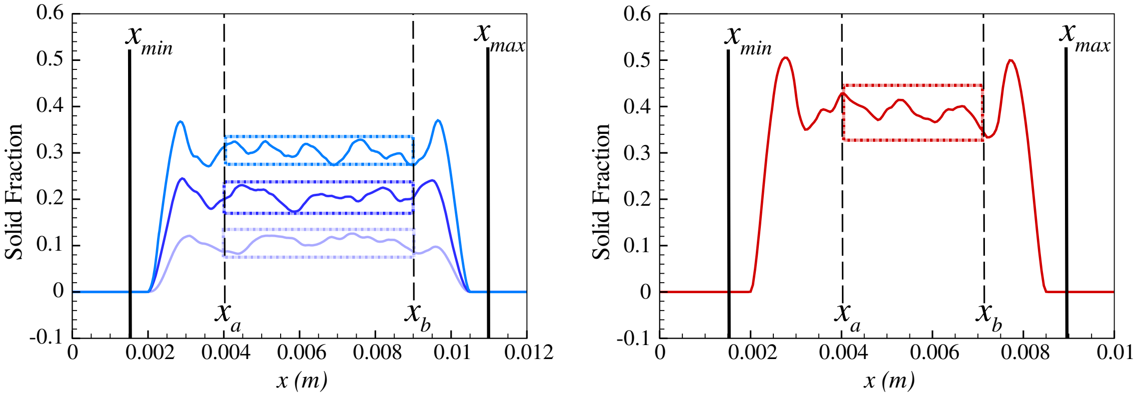

Fig. 7 Solid volume fraction distribution along the axial flow direction, with box showing homogeneous regions of the bed where heat transfer coefficients are computed

In the configuration chosen in this study, the temperature of the fluid increases in the streamwise direction because of the heat transferred from the solid phase. In order to study the mean temperature evolutions in space, we define a mean cross-sectional fluid temperature

$$T_{\mathrm{f}}(x) = \frac{\iint\limits_{S} \chi(x, y, z) T(x, y, z) \mathrm{d}y\mathrm{d}z}{\iint\limits_{S} \chi(x, y, z) \mathrm{d}y\mathrm{d}z}, \tag{48}$$

and a mean cross-sectional bulk temperature (with u the streamwise velocity component)

$$T_{\mathrm{b}}(x) = \frac{\iint\limits_{S} \chi(x, y, z) u(x, y, z) T(x, y, z) \mathrm{d}y\mathrm{d}z}{\iint\limits_{S} \chi(x, y, z) u(x, y, z) \mathrm{d}y\mathrm{d}z}, \tag{49}$$

by surface (instead of volume) integrals over the cross-sectional area S, which represents the section of the computational domain orthogonal to the streamwise direction. The volume integral quantities approach the surface integrals when $\mathrm{d}x \to 0$. The mean cross-sectional solid volume fraction and fluid velocity are then

$$\phi_{\mathrm{s}}(x) = \iint\limits_{S} (1 - \chi)(x, y, z) \mathrm{d}y\mathrm{d}z \quad \text{and} \quad U_{\mathrm{f}}(x) = \frac{\iint\limits_{S} \chi(x, y, z) u(x, y, z) \mathrm{d}y\mathrm{d}z}{\iint\limits_{S} \chi(x, y, z) \mathrm{d}y\mathrm{d}z}. \tag{50}$$

Figure 7 shows the streamwise profiles of the mean cross-sectional solid volume fraction for all the numerical simulations. Entrance, packed and exit zones are clearly highlighted. In addition to the inlet and outlet x coordinates, we define $x_{min} = x_{\mathrm{In}} + 1.5\, d_{\mathrm{p}}$ and $x_{\mathrm{max}} = x_{\mathrm{Out}} - 1\, d_{\mathrm{p}}$ as the coordinates of a domain containing all the particles and for which the temperature gradient is null at the boundaries, and $x_{\mathrm{a}} = x_{\mathrm{In}} + 4\, d_{\mathrm{p}}$ and $x_{\mathrm{b}} = x_{\mathrm{Out}} - 3\, d_{\mathrm{p}}$ as the coordinates of a reduced domain inside which the solid volume fraction may be considered as homogeneous. Figure 8 shows the temperature and the streamwise velocity fields of the fluid flowing through the fixed array of particles, at Reynolds number $Re = 50$ and solid volume fraction $\phi_{\mathrm{s}} = 0.2$, on a slice taken in the middle of the box. The interactions of particle wakes, which modify the velocity and the temperature fields, clearly appear on the visualizations. The temperature is higher inside the boundary layer around each particle, and it is higher downstream of each particle because of the wake effects. Temperature and velocity are anticipated to be correlated. High velocity between particles is expected because of mass flux conservation. This participates to enhancement of heat transfer from the particle surface. In order to investigate this point, the spatial occurrence density function (SDF), $f(u^*, T)$, and the average of the temperature conditioned on the normalized streamwise velocity $u^* = u/U_{\mathrm{In}}$, $< T|u^* >_{\mathrm{f}}$, are computed for the same case shown in Fig. 8. Both statistical quantities are evaluated over a slice in the middle of the box, bounded between x_{a} and x_{b} in order to avoid single phase zones, withdrawing the points at 320 K which correspond to the solid border and its interior.

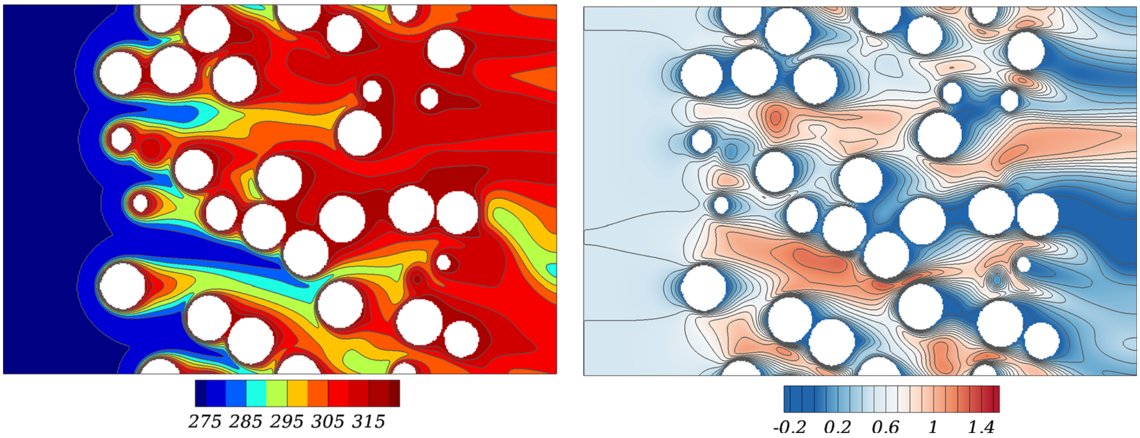

Fig. 8 Temperature and streamwise velocity fields around the particles, at $Re = 50$ and $\phi_s = 0.2$, in the middle of the box

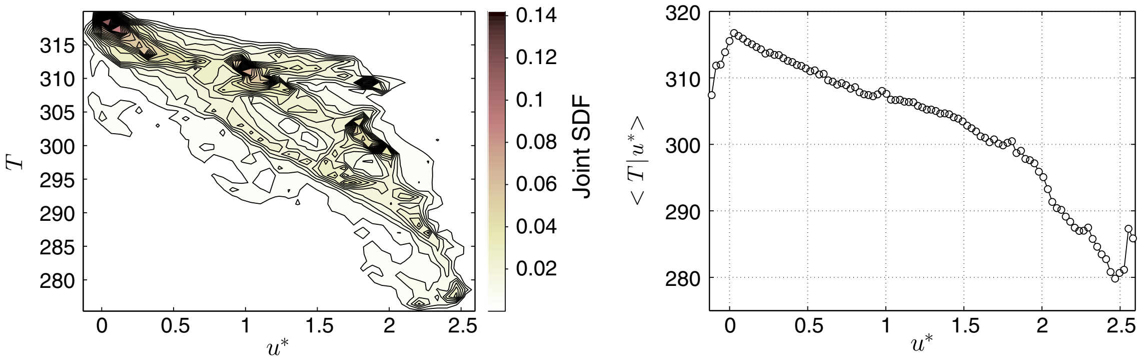

Fig. 9 Joint SDF of fluid streamwise velocity and temperature (left) and conditional average of fluid temperature on fluid streamwise velocity (right) at $Re = 50$ and $\phi_s = 0.2$

Results, displayed in Fig. 9, show that temperature and velocity are indeed correlated. Higher occurrences are found in the zones corresponding to low fluid velocity that is close to the particle surface or between neighboring particles whose arrangement promote recirculation zones with stagnation points. High occurrences are also found at the velocity corresponding to the flow rate (0.5 m/s) and near to the exit region. Decreasing the solid volume fraction makes to move the maximum of occurrences toward high-velocity and low-temperature zones which corresponds to those regions in which the particle–particle interactions are low, whereas increasing the solid volume fraction increases the occurrence at very low fluid velocity and high temperatures, as shown in Fig. 10. Temperature–velocity correlations also vary with the Reynolds number, as shown in Fig. 11. Correlation coefficients between temperature and velocity were found to be −0.65, −0.78 and −0.81 at Reynolds numbers 10, 50 and 100, respectively, for $\phi_s = 0.2$. These differences are expected as they rely on the residence time of the fluid within the fixed assembly of particles, at the different Reynolds numbers simulated in this study. The transient evolution of the mean cross-sectional bulk temperature $T_b(x)$ and the mean cross-sectional fluid temperature $T_f(x)$ are plotted in Fig. 12, for the case $Re = 50$ and $\phi_s = 0.4$. Results show that a steady state is reached for these laminar conditions. Results also point out some differences in the two steady temperature profiles. Within the fixed bed, T_f turns out to be greater than T_b and less smooth. This is consistent with the two different definitions. T_b is indeed obtained from a weighted average by the local fluid velocity. It was previously shown that higher temperatures correspond to lower velocities in the bed. Moreover, low velocity zones mainly correspond to those zones in which particle wakes interact with each others because of the particle proximity; these interactions break down the flow and lead to recirculation effects which affect the fluid flowing through the fixed array, and the temperature as well. It is reasonable to suppose that such interactions induce some disturbances in the spatial evolution of the fluid temperature, leading to a less smooth profile.

Keeping these results in mind, we now compute the heat transferred from the solid to the fluid phase in order to further evaluate the two Nusselt numbers (Eqs. 43, 45) which make it possible to model such a heat exchange. The heat transfer rate may be computed using two different methods (Eqs. 30, 31) which should yield

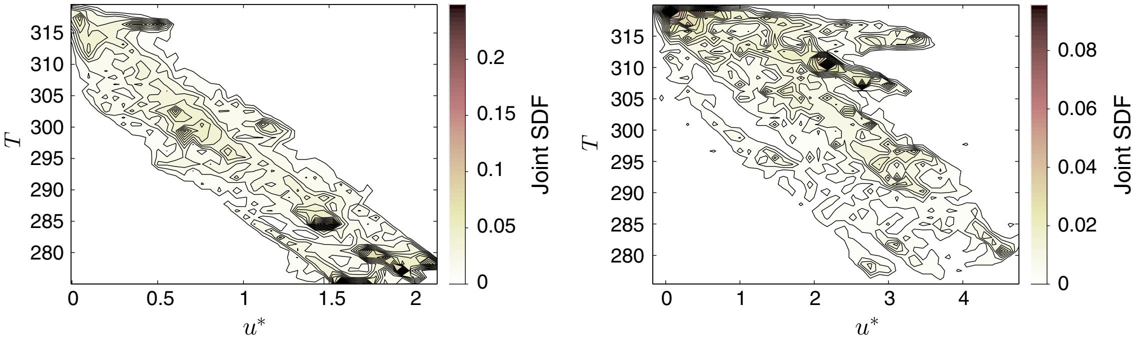

Fig. 10 Joint SDF of fluid streamwise velocity and temperature at $Re = 50$ for $\phi_s = 0.1$ (left) and $\phi_s = 0.4$ (right)

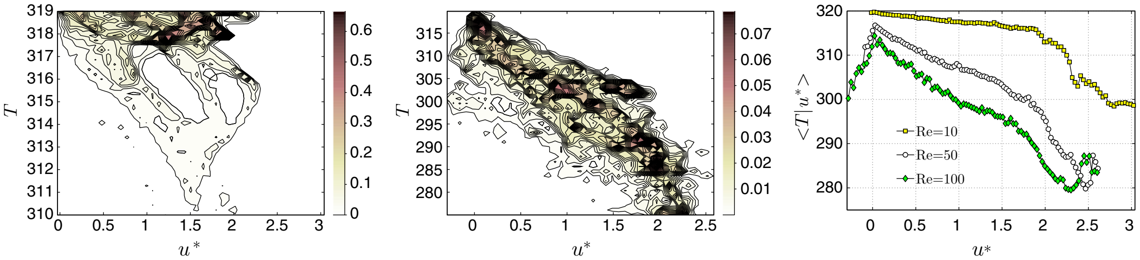

Fig. 11 Joint SDF at $Re = 10$ (left) and $Re = 100$ (center); conditional average (right) for all the Reynolds numbers. Statistical quantities evaluated for $\phi_s = 0.2$

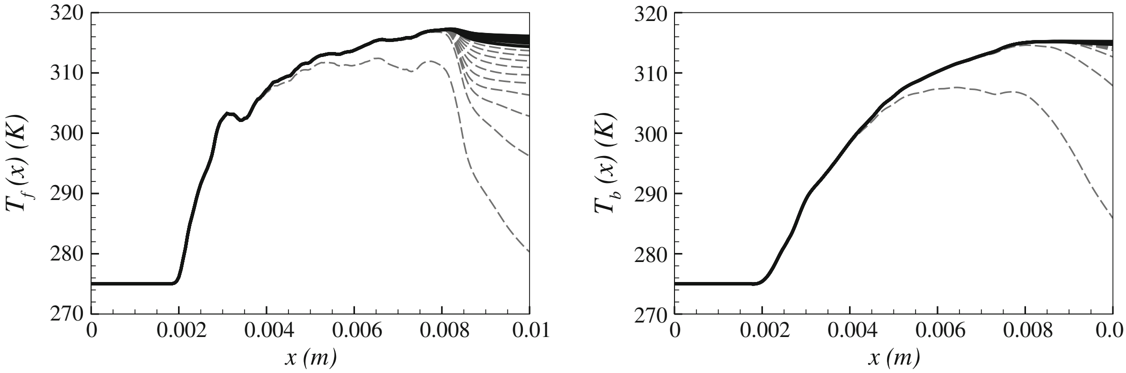

Fig. 12 Temperatures evolutions: $T_f(x)$ (left) and $T_b(x)$ (right) at $Re = 50$ and $\phi = 0.4$

identical results provided that the same domain is used and the entire exchanging surface of each particle is accounted for. In order to compare numerical simulations using different numbers of particles, N_p, normalized heat transfer rate are defined as follows: $\widehat{Q}_f = Q_f/N_p$ and $\widehat{Q}_p = Q_p/N_p$, where Q_p and Q_f correspond to $Q_{p\rightarrow f}$ as defined by Eqs. (30) and (31), respectively. To compute $Q_p^{(k)}$, for each particle k, the algorithm presented in Sect. 3 cannot be used. Such an algorithm indeed requires a sufficient number of grid points in the normal direction to each interface, in order to accurately approximate the temperature gradient on each particle surface. For a quite coarse mesh, in the presence of particles very close to each others, such a number is not ensured with the consequence that the numerical accuracy is low. Each particle heat rate is thus computed using a cubic box of length $d_p + 2dx$, centered on the particle mass center. The whole heat rate is obtained as follows:

$$Q_p = \sum_{k=1}^{N_p} \left(\iint_{S_{\text{box}}} \rho_f C_p T \mathbf{u} \cdot \mathbf{n} \, dS + \iint_{S_{\text{box}}} -k_f \nabla T \cdot \mathbf{n} \, dS \right), \tag{51}$$

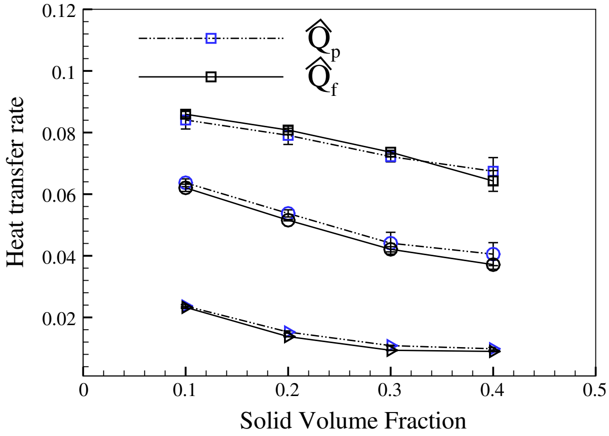

Fig. 13 Heat transfer rate for different particle concentration, at $Re = 10$ ▷, $Re = 50$ ○, and $Re = 100$ □

where S_{box} is the total box surface. In order to compare the two methods (Eqs. (30), (31)) a domain bounded by $x_{\min}, x_{\max}$ is chosen and Q_{f} computed as

$$Q_{\text{f}} = \left(\iint\limits_{S_{\min}} \chi \rho_{\text{f}} C_{\text{p}} T \mathbf{u} \cdot \mathbf{n} \, \mathrm{d}S + \iint\limits_{S_{\max}} \chi \rho_{\text{f}} C_{\text{p}} T \mathbf{u} \cdot \mathbf{n} \, \mathrm{d}S \right), \tag{52}$$

where $S_{\min} = S$ and $S_{\max} = S$ are, respectively, the inlet and the outlet cross-sectional areas at the positions $x_{\min}$ and $x_{\max}$, since periodic boundary conditions in spanwise directions of the computational domain are imposed. At such locations, the temperature gradient is almost zero and the heat transfer rate may be computed without accounting for the conduction contribution.

For all the numerical simulations of the present study, $\widehat{Q}_{\text{p}}$ and $\widehat{Q}_{\text{f}}$ are computed and averaged over five realizations differing each other by the random particle arrangements. Averaged results and standard deviations are presented in Fig. 13. The latter shows that for each Reynolds number and solid volume fraction, the two methods give very close results and may be both employed for estimating the total heat transfer rate. The method computing the heat exchanged from individual particle with the surrounding fluid is indeed useful for analyzing the heat transfer rate statistical dispersion. The relative occurrence of $Q_{\text{p}}^{(k)}$ is computed over the five realizations of each test case and results displayed in Fig. 14. Simulations show a large dispersion corresponding to higher solid volume fractions, for all the Reynolds numbers, thus proving the limits of Eulerian or Lagrangian methods to accurately reproduce such interactions at larger scales assuming homogeneous quantities in a same volume of control. This is a clear signature of the interplay between local heat transfer and the microstructure of the particle spatial distribution.

Alternatively to Eq. (30), Eq. (31) may be used for computing the heat transferred from the solid to the fluid phase in a reduced domain where bounding surfaces cut the particle interface. In computing the total rate of heat transfer in such a reduced domain, both the convection and the conduction contributions should be taken into account. The two contributions

$$Q_{fcd} = \iint\limits_{S_{\text{a}}} -\chi k_{\text{f}} \nabla T \cdot \mathbf{n} \, \mathrm{d}S + \iint\limits_{S_{\text{b}}} -\chi k_{\text{f}} \nabla T \cdot \mathbf{n} \, \mathrm{d}S, \tag{53}$$

$$Q_{fcv} = \iint\limits_{S_{\text{a}}} \chi \rho_{\text{f}} C_{\text{p}} T \mathbf{u} \cdot \mathbf{n} \, \mathrm{d}S + \iint\limits_{S_{\text{b}}} \chi \rho_{\text{f}} C_{\text{p}} T \mathbf{u} \cdot \mathbf{n} \, \mathrm{d}S \tag{54}$$

are evaluated over the five realizations carried out for each numerical test case, within the domain bounding by the streamwise coordinates x_{a} and x_{b} (with $S_{\text{a}} = S_{\text{b}} = S$). Their ratio is depicted in Fig. 15. It increases by decreasing the Reynolds number and by increasing the solid volume fraction as well. For the lowest Reynolds number simulated in this study, its mean value is found to be lower than 0.03, and even smaller for the two higher Reynolds numbers (< 0.007, < 0.004). The conductive contribution is therefore small enough to be

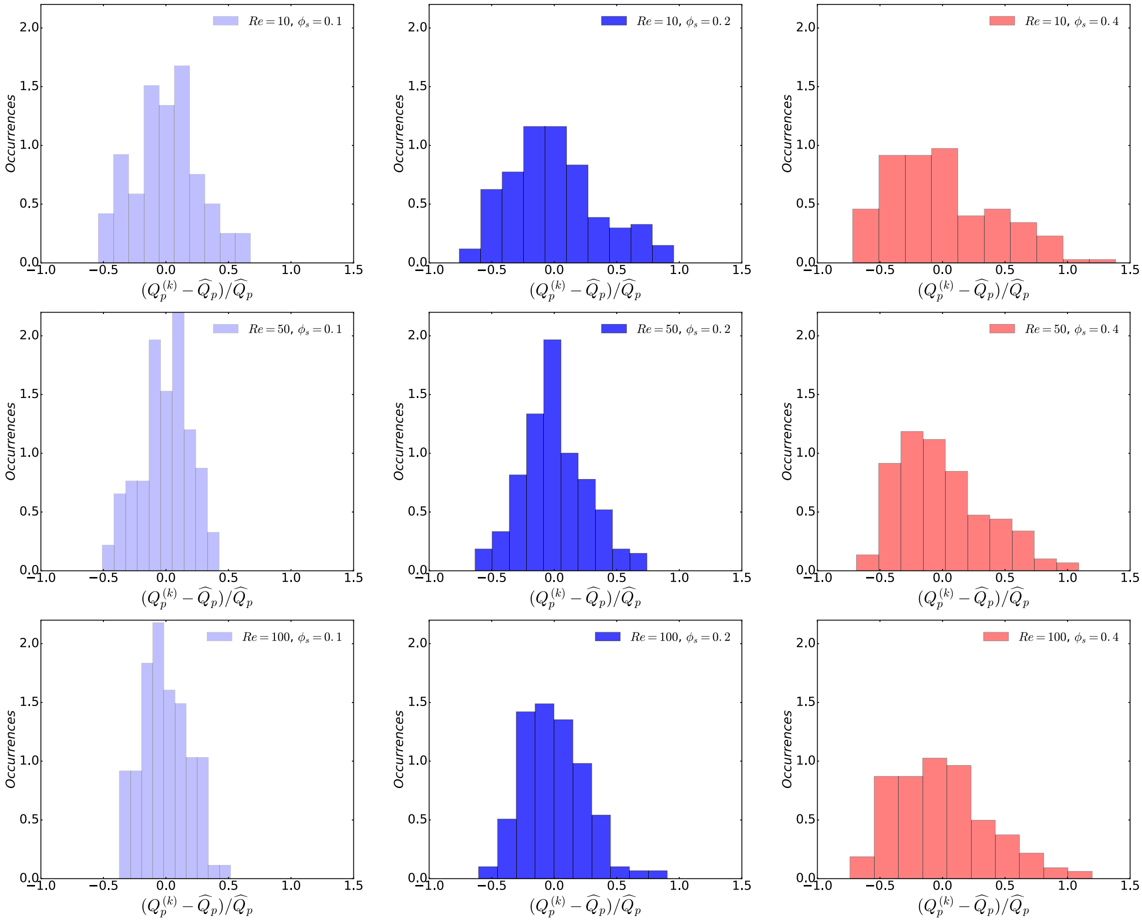

Fig. 14 Distribution of single particle heat transfer rate $Q_{\mathrm{p}}^{(k)}$

neglected in the present study (while it should not be for lower Reynolds number, as also recently demonstrated by Sun et al. [34]). By the reduced domain, which is considered homogeneous with regard to the solid volume fraction, the heat transfer coefficients may be estimated by Eqs. (42) and (46), defining the global solid surface (instead of the surface per unit volume) as $(6\phi_{\mathrm{s}}/d_{\mathrm{p}})S(x_{\mathrm{b}} - x_{\mathrm{a}})$, where ϕ_{s} is the averaged solid volume fraction computed as $\phi_{\mathrm{s}} = \frac{1}{x_{\mathrm{b}} - x_{\mathrm{a}}} \int_{x_{\mathrm{a}}}^{x_{\mathrm{b}}} \phi_{\mathrm{s}}(x)\mathrm{d}x$ (or, equivalently, by the volume average over the reduced volume). The two Nusselt numbers are then obtained using their definitions (Eqs. (43), (45)).

In the literature, several correlations for the Nusselt number have been proposed. Three of them are recalled below:
Gunn [2]

$$\mathrm{Nu} = \left(7 - 10\phi_{\mathrm{f}} + 5\phi_{\mathrm{f}}^2\right)\left(1 + 0.7Re^{0.2}Pr^{1/3}\right) + \left(1.33 - 2.4\phi_{\mathrm{f}} + 1.2\phi_{\mathrm{f}}^2\right)Re^{0.7}Pr^{1/3}, \tag{55}$$

Deen et al. [8]

$$\mathrm{Nu} = \left(7 - 10\phi_{\mathrm{f}} + 5\phi_{\mathrm{f}}^2\right)\left(1 + 0.17Re^{0.2}Pr^{1/3}\right) + \left(1.33 - 2.31\phi_{\mathrm{f}} + 1.16\phi_{\mathrm{f}}^2\right)Re^{0.7}Pr^{1/3}, \tag{56}$$

Sun et al. [10]

$$\mathrm{Nu} = \left(-0.46 + 1.77\phi_{\mathrm{f}} + 0.69\phi_{\mathrm{f}}^2\right)/\phi_{\mathrm{f}}^3 + \left(1.37 - 2.4\phi_{\mathrm{f}} + 1.2\phi_{\mathrm{f}}^2\right)Re^{0.7}Pr^{1/3}. \tag{57}$$

These correlations are used for a comparison purpose and further employed for a modeling purpose. Nusselt numbers are computed for all the numerical test cases by averaging over the five realizations of each case. Figure 16 (left) shows the averaged Nusselt number Nu_{b} compared with the correlations proposed by Deen et al. [8] and Sun et al. [10]. In Fig. 16 (right), the averaged Nusselt number Nu_{f} is instead compared with Gunn's

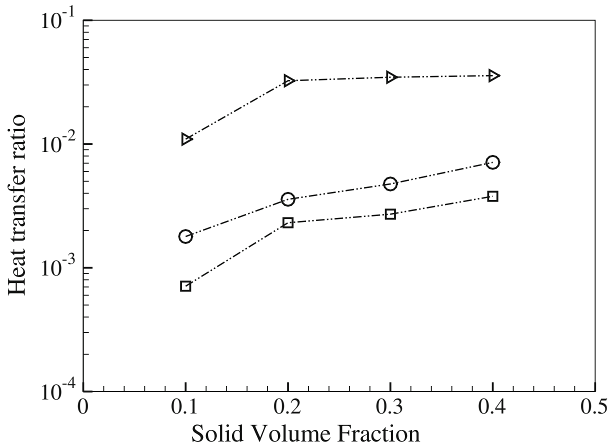

Fig. 15 Q_{fcd}/Q_{fcv} assessed in the homogeneous region of the particle arrays at $Re = 10$ ▷, $Re = 50$ ◯, and $Re = 100$ ☐

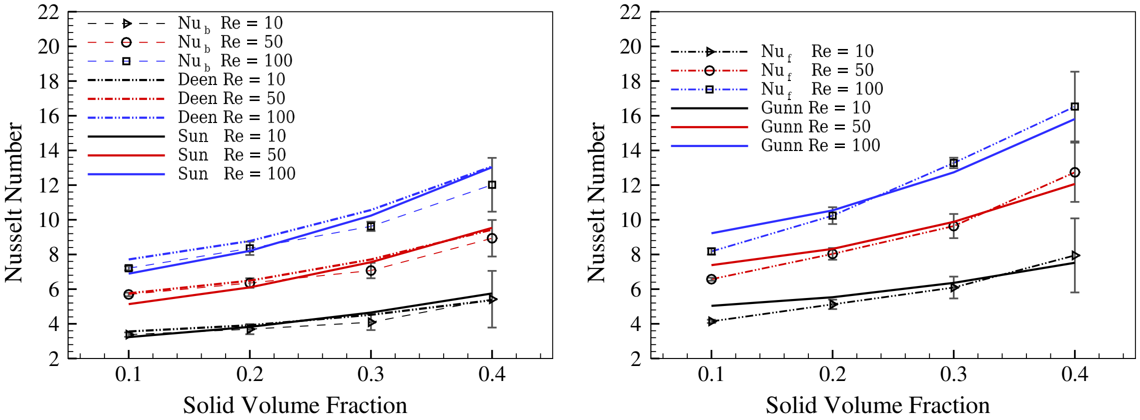

Fig. 16 Nusselt numbers computed from our numerical simulations, compared with the correlations of the literature: $\mathrm{Nu_b}$ (45), Deen et al. [8] and Sun et al. [10] (left); $\mathrm{Nu_f}$ (43), Gunn [2] (right). $Re = 10$ ▷, $Re = 50$ ◯, and $Re = 100$ ☐

correlation [2]. Results show that $\mathrm{Nu_b}$ estimated in the present study compares well with the correlations of the literature, which are obtained by fully resolved particle numerical simulations using the same definition (based on the bulk temperature). It is worth noting that $\mathrm{Nu_f}$ computed in the present work is instead closer to the Gunn correlation. Gunn [2] used the bulk temperature in his analytical approximated formulation to derive asymptotic values for the Nusselt number. However, the proposed correlation was further obtained on the basis of available data from the literature, while the definition of the temperature used in the Nusselt number estimate is not clear.

Recent studies carried out on random fixed particle arrays [6, 9–11] all showed that the correlation proposed by Gunn [2] overestimates the numerical Nusselt predictions. These studies used the bulk temperature in the Nusselt number formulation. Comparing $\mathrm{Nu_b}$ with the Gunn correlation, our results lead to the same conclusion. However, when the $\mathrm{Nu_f}$ is assessed, the Gunn correlation is found to overpredict only the lowest solid volume fraction while globally agreeing with the numerical results. A good agreement with the Gunn correlation was recently pointed out from the experiments by Buist et al. [35]. The sensitivity of the two Nusselt numbers in the present configuration was investigated over three grid sizes and four test cases. Results are shown in Fig. 17. In the worst case ($Re = 50$, $\phi_s = 0.4$), extrapolating the predictions from $N_d = 20$ to $N_d = 60$, an error of about 13% is found for $\mathrm{Nu_f}$. It is worth noting that the ratio $\mathrm{Nu_f}/\mathrm{Nu_b}$ is instead insensitive to the mesh size and may be considered independent of numerical errors (only affected by statistical errors due to the sampling).

In Sect. 4.2, we demonstrated that the ratio between the two Nusselt numbers is strictly equivalent to the ratio between the solid-to-fluid and the solid-to-bulk temperature differences. Equation (47) is indeed proved by the numerical results shown in Fig. 18. The direct consequence of such a relation is that if T_f and the two Nusselt numbers are known, then T_b is known as well. This information is extremely useful in the frame of

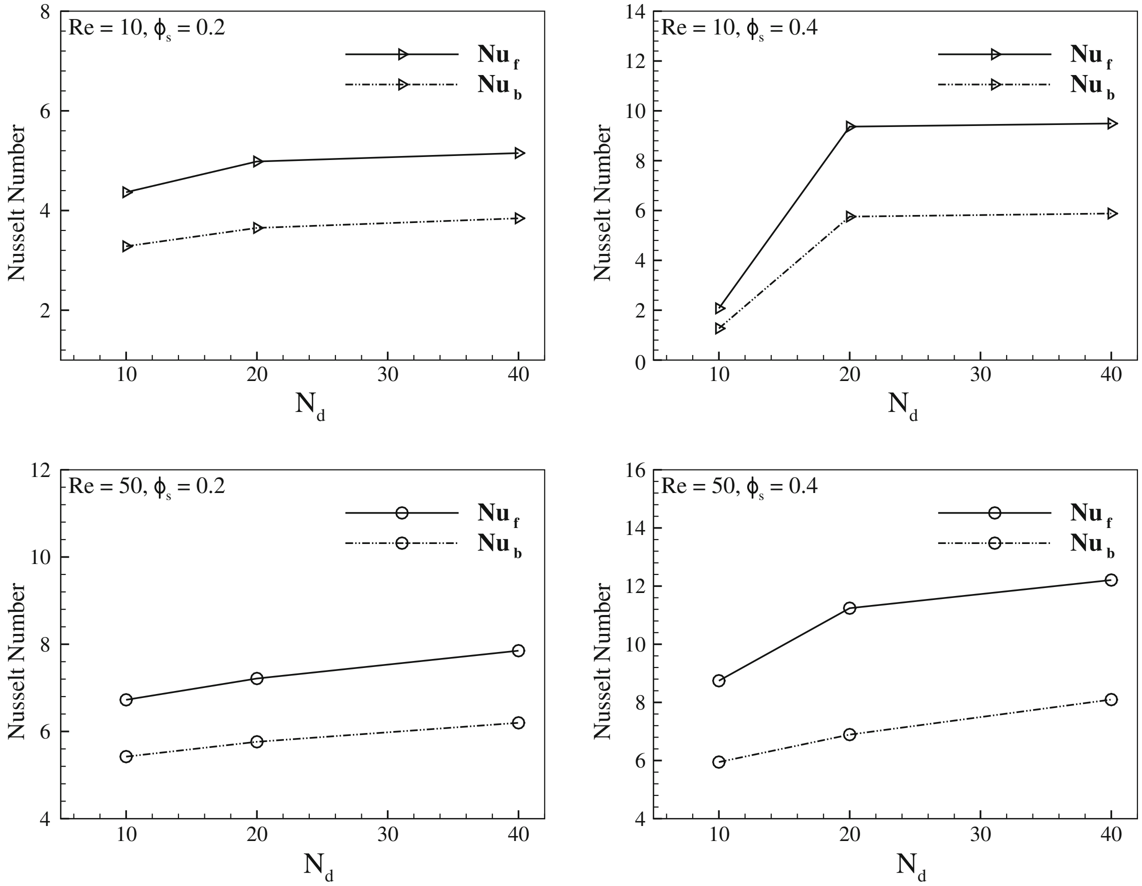

Fig. 17 Nusselt numbers $\mathrm{Nu_f}$ and $\mathrm{Nu_b}$ for different grid sizes

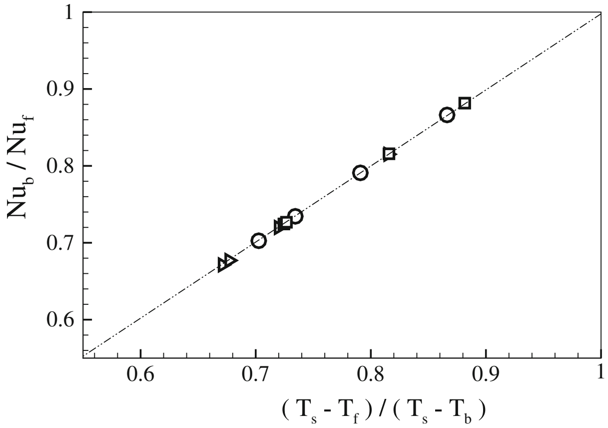

Fig. 18 Ratio of Nusselt numbers versus ratio of temperature differences

an Eulerian–Eulerian approach as it provides a closure for the fluctuating velocity–temperature correlation appearing in the energy conservation equation (39). From Eq. (38), we indeed obtained

$$-\langle T'\mathbf{u}'\rangle_\mathrm{f} = (T_\mathrm{f}\mathbb{I} - \mathbb{T}_\mathrm{b}) \cdot \mathbf{U}_\mathrm{f}, \tag{58}$$

which, according to the mean flow direction of our simulations, reduces to

$$-\langle T'u'\rangle_\mathrm{f} = (T_\mathrm{f} - T_\mathrm{b})U_\mathrm{f}, \tag{59}$$

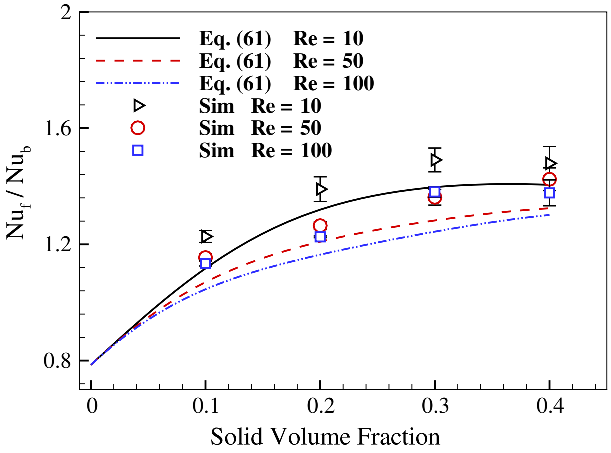

Fig. 19 Nusselt ratio computed from the numerical simulations and modeled by Eq. (61)

with the fluid-to-bulk temperature difference modeled as

$$T_\mathrm{f} - T_\mathrm{b} = (T_\mathrm{s} - T_\mathrm{f})\left(\frac{\mathrm{Nu_f}}{\mathrm{Nu_b}} - 1\right). \tag{60}$$

Therefore, knowing the ratio between $\mathrm{Nu_f}$ and $\mathrm{Nu_b}$ makes it possible to close the pseudo-turbulent heat flux. This reasonably applies to all those flows in which a main direction may be identified. Likewise, knowing $\mathrm{Nu_f}$ ensures a consistent formulation of the two-phase flow heat exchanges.

In a recent work, Sun et al. [10] proposed to model the solid-to-fluid heat transfer rate by using $\mathrm{Nu_b}$ together with an extra term which relates the fluid temperature T_f to the bulk temperature T_b, obtained by fitting their data. So doing, they in fact provided a model for $\mathrm{Nu_f}$ from which the ratio $\mathrm{Nu_f}/\mathrm{Nu_b}$ may straightforwardly be obtained as follows:

$$\frac{\mathrm{Nu_f}}{\mathrm{Nu_b}} = \frac{\pi}{4\left[1 - 1.6\phi_\mathrm{s}\phi_\mathrm{f} - 3\phi_\mathrm{s}\phi_\mathrm{f}^4 \exp(-Re^{0.4}\phi_\mathrm{s})\right]}. \tag{61}$$

Such a ratio is here assessed from the numerical simulations and results are displayed in Fig. 19. In the latter, predictions obtained from Eq. (61) are also given for a comparison purpose. Figure 19 shows that the Nusselt ratio decreases with the Reynolds number and increases with the solid volume fraction. This is explained by the fact that the higher is the Reynolds number, the thinner is the particle boundary layer and therefore the smaller is the difference between T_f and T_b. Conversely, the larger is the solid volume fraction, the higher are the wake interactions, which promote stagnation zones between neighboring particles, thus leading to magnifying the temperature difference. Figure 19 also shows that this trend is well captured by the model (Eq. (61)). Such a model is therefore used in conjunction with the two aforementioned correlations [8,10] and compared with the $\mathrm{Nu_f}$ obtained by our numerical simulations. For the sake of conciseness, we will refer to as $\mathrm{Nu_D}$ for the product between $\mathrm{Nu_b}$ proposed by Deen et al. [8] and the correlation $\mathrm{Nu_f}/\mathrm{Nu_b}$ given by Eq. (61), and to as Nu_S for the product between $\mathrm{Nu_b}$ proposed by Sun et al. [10] and the same correlation. (The latter represents the corrected model proposed by those authors, which we refer to as $\mathrm{Nu_f}$.) Results are displayed in Fig. 20. A very good agreement is found between the numerical results and the correlations from the literature when the fluid-to-bulk Nusselt ratio is used. Only slight differences are observed at the lowest solid volume fraction and high Reynolds numbers. For very low volume fraction regimes, in the limit of $\phi_\mathrm{s} \to 0$, the Nusselt ratio correlation (Eq. (61)) should tend to unity, while it does not. When the solid volume fraction approaches the typical values of dilute regimes ($\sim 1\%$), using such a correlation would entail under-predicting the heat exchanges between solid and fluid phases. In some industrial applications, these low volume fractions occur in zones in which an accurate prediction of the heat transfers is crucial (for example, in the freeboard region of reactive fluidized beds [36]). Having a suitable correlation which may be used in both dense and dilute regimes is still an open question which should be addressed. Outside these regimes, the model provides very satisfactory results in predicting $\mathrm{Nu_f}$ based on the $\mathrm{Nu_b}$ from literature. Its ability to predict the fluctuating velocity–temperature contribution, or pseudo-turbulent heat flux, is evaluated below. This quantity is assessed

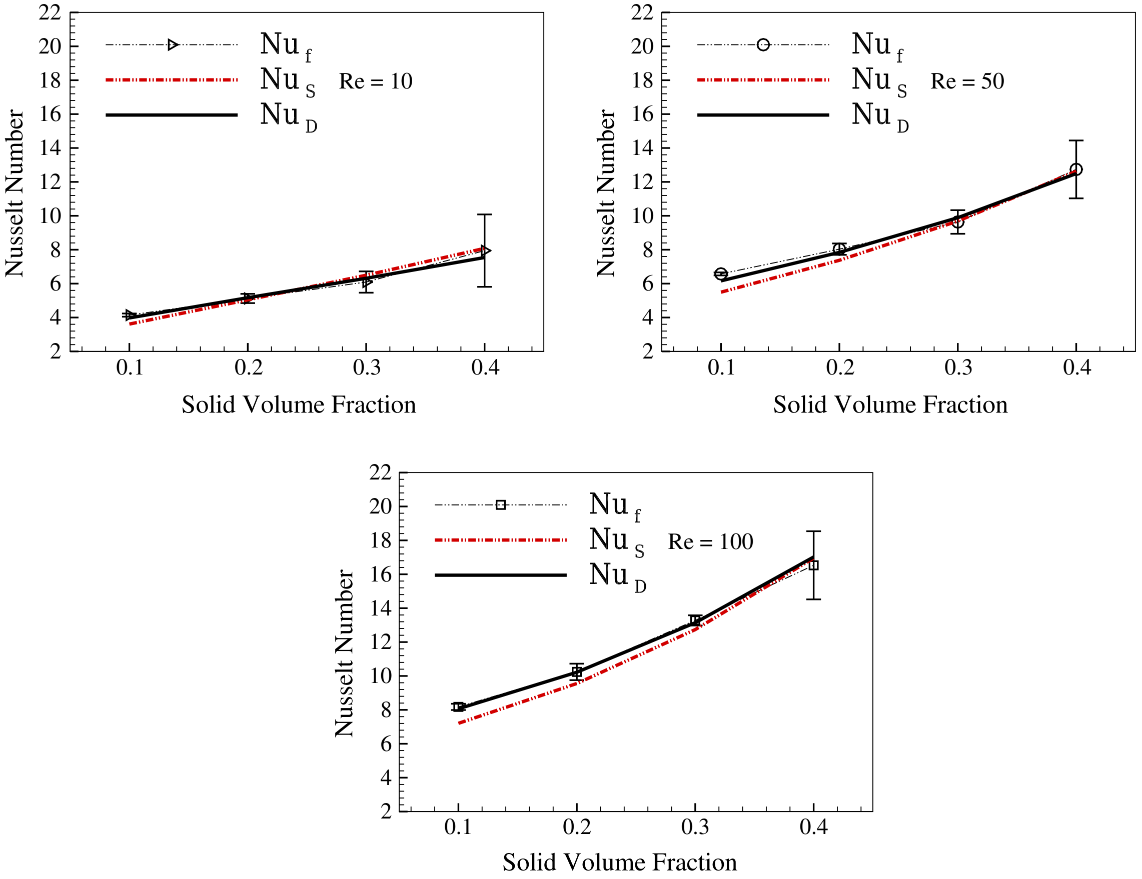

Fig. 20 $\mathrm{Nu_f}$ as obtained by the present study compared with $\mathrm{Nu_D}$ and $\mathrm{Nu_s}$ computed by the correlations of the literature using Eq. (61)

using our direct numerical simulations, and Eq. (59) is verified along the streamwise direction. Results are shown in Figs. 21, 22 and 23 for Reynolds numbers 10, 50 and 100, respectively. For all the test cases, the fluctuating velocity–temperature contribution increases with the solid volume fraction at the beginning of the packed zone and then decreases toward the exit zone. This is consistent with a decrease in the temperature gradient in the homogeneous region of the bed. Such a decrease is significant at the lowest Reynolds number and the highest solid volume fraction; it is instead weaker at higher Reynolds numbers, especially for low ϕ_s. Results also show that the higher is the Reynolds number and/or the solid volume fraction, the larger is its intensity. This pseudo-turbulent heat flux indeed accounts for the correlation between fluid velocity and temperature fluctuations induced by the particles and represents a local flow disturbance due to the wake interactions of neighboring particles. Contrary to the turbulent effects, it is a small-scale phenomenon which depends on the microstructure of the particulate flow, as well as on the solid volume fraction and the thermo-hydrodynamic characteristics of the mixture. It may have a substantial effect on dense particle-laden flows and should be taken into account in the modeling. The importance of this contribution was pointed out by a recent work of Sun et al. [34]. The ability of the Nusselt number ratio to reproduce the pseudo-turbulent heat flux is investigated by computing the fluctuating velocity–temperature correlations from Eqs. (59) and (60) using $\mathrm{Nu_f}/\mathrm{Nu_b}$ estimated from the numerical simulations and modeled by Eq. (61). The latter is computed by using the mean value of the solid volume fraction in the homogeneous packed zone. The former is obtained using averaged Nusselt numbers (i.e., one value for each operating point). Obviously, integrating Eq. (36) over the spanwise directions and alternately accounting for Eqs. (41) and (44) make it possible to obtain a Nusselt ratio which is function of the streamwise coordinate. Using this ratio leads the exact reproduction of the actual fluctuating velocity–temperature term (not shown). This operation is rather a numerical validation and it is not interesting from a modeling point of view. This is why averaged Nusselt numbers over x are instead used. Both the predictions are only evaluated within the packed zone. A comparison with the actual contribution computed

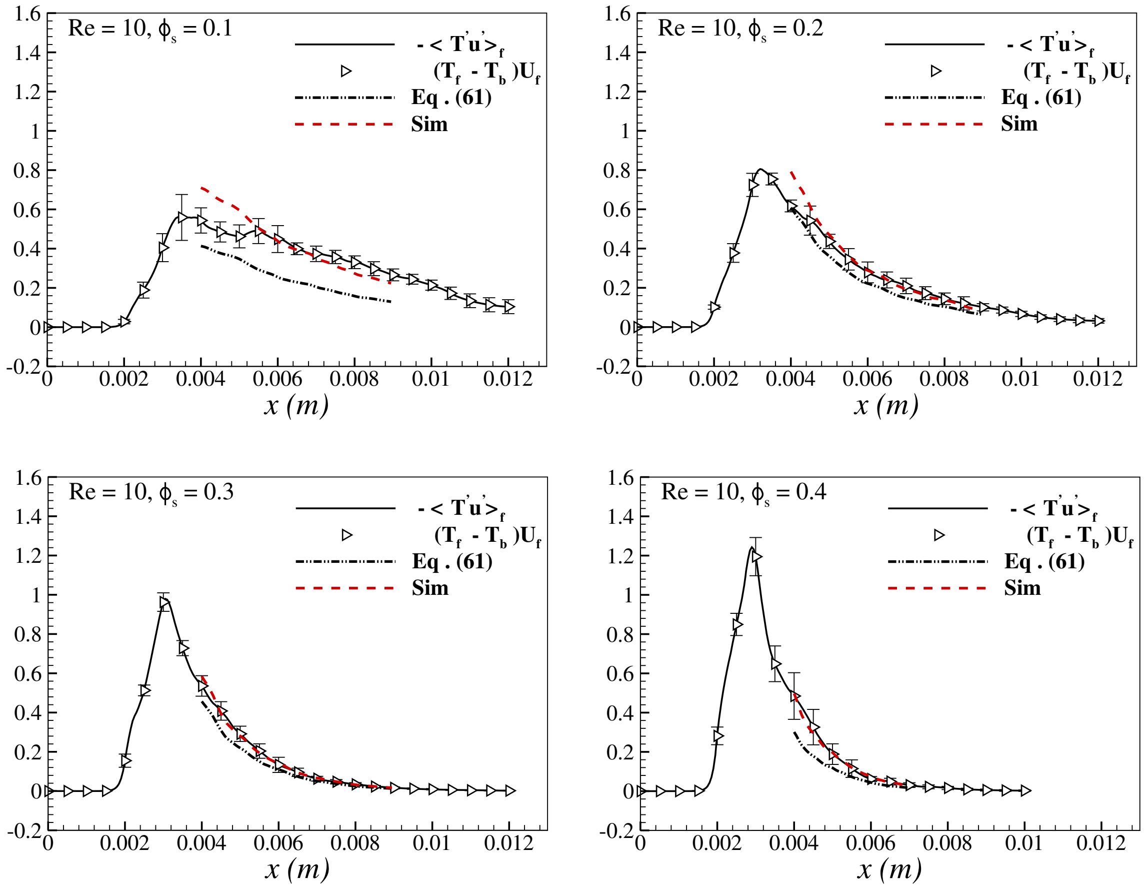

Fig. 21 Pseudo-turbulent heat flux, $-\langle T'u'\rangle_{\mathrm{f}}$, computed using the numerical simulations from the fluctuating velocity–temperature averages (solid line) and from $(T_{\mathrm{f}} - T_{\mathrm{b}})U_{\mathrm{f}}$ according to Eq. (59) (symbols), and modeled by Eq. (60) using the ratio $\mathrm{Nu}_{\mathrm{f}}/\mathrm{Nu}_{\mathrm{b}}$ estimated by the numerical simulations (dashed red line) and by Eq. (61) (dot dashed black line), at $Re = 10$

from the numerical simulations is given in Figs. 21, 22, 23. The modeling based on the ratio estimated from the numerical simulations shows a very good agreement with the measured quantity. The modeling based on Eq. (61) also provides satisfactory results even if slightly under-predicting the numerical measurements. We observe, however, a larger underestimation corresponding to the lowest volume fraction for all the Reynolds numbers. This observation is consistent with our previous considerations about the inability of the correlation to reproduce volume fraction regimes corresponding to dilute regime $\phi_{\mathrm{s}} \to 0$. We believe that this represents an important point which deserves further studies characterizing such a transition from dilute to dense flows.

5 Conclusion

In the present study, particle-resolved direct numerical simulations were performed from a single sphere to an assembly of random particles in order to characterize the heat transfer in dense gas-particle flows. A Lagrangian VOF approach using fictitious domains and combined with a penalty method was used to solve the fluid and its interactions with the solid phase. This approach uses a Lagrangian tracking for the phase function together with a second-order implicit tensorial penalty method (ITPM) when solving cases with moving particles. An augmented Lagrangian method is also employed in order to ensure incompressibility when dealing with the multiphase problems. In the present study, since fixed particles were simulated the alternatively Darcy penalty method (DPM) was used. The first part of the present study concerned the validation of the numerical strategy employed for obtaining the heat transfer coefficients and the related Nusselt numbers. The latter were analyzed on a single solid sphere over two well-known test cases: a pure heat diffusion from a hot particle to a quiescent cold fluid and a diffusion/convection heat transfer from a hot particle to a laminar fluid flow. The first test case,

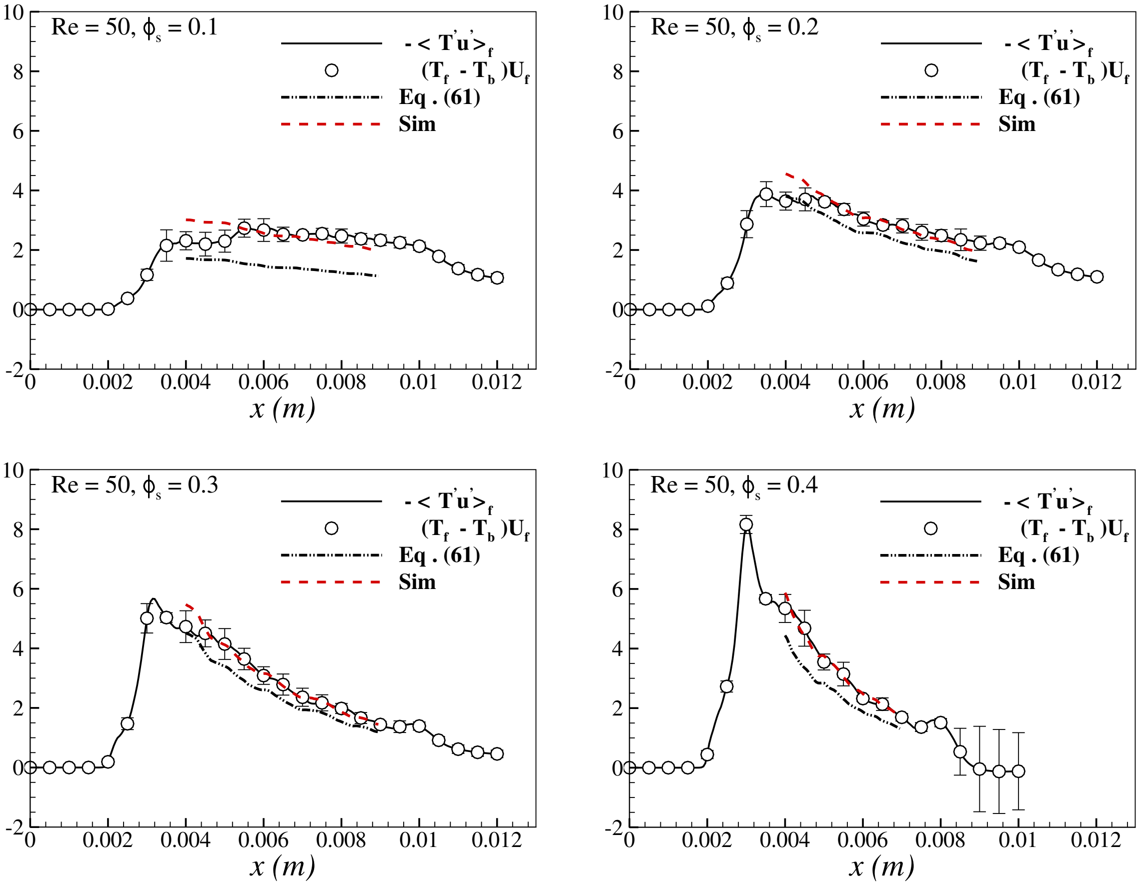

Fig. 22 Pseudo-turbulent heat flux. Same caption as in Fig. 21, at $Re = 50$

for which an analytical solution is available, made it possible to verify both the ability of the numerical method to accurately solve the heat exchange near the interfaces and the ability of the post-processing algorithm to compute the heat flux around the sphere. The second test case additionally allowed the verification of an alternative method for estimating the heat transfer rate using an inlet–outlet integral heat balance. The second part of this work was devoted to the analysis of the heat transfer occurring between the particles and the fluid in an assembly of random motionless spherical particles. Using the fully resolved numerical simulation, three Reynolds numbers ($\in$ [10, 100]) and four solid volume fractions ($\in$ [0.1, 0.4]), for unity Prandtl number, were investigated. For each numerical test case, the heat transfer rate was computed and two Nusselt numbers, based, respectively, on the fluid temperature and on the bulk (cup-mixing) temperature, were obtained and analyzed. Numerical results revealed some differences between such Nusselt numbers for the same operating point. The specificity of the two Nusselt numbers was put forward and the inadequacy of the one based on the bulk temperature to close the heat exchanges between the phases in an Eulerian–Eulerian approach was pointed out. Finally, based on a Eulerian–Eulerian formulation of the fluid energy equation, a connection between the ratio of the two Nusselt numbers and the fluid velocity–temperature covariance was identified. The latter (also referred to as pseudo-turbulent heat flux in the literature) accounts for the velocity and temperature fluctuations induced by the particles on the fluid and represents a small-scale phenomenon which depends on the local microstructure of the particulate flow, as well as on the solid concentration and the thermo-hydrodynamic characteristics of the mixture. Its connection with the Nusselt number ratio made it possible to obtain a closure based on the available correlations from the literature. Such a closure was tested in the present configuration corresponding to a mean steady flow aligned to the mean temperature gradient. Preliminary successfully tests have also been carried out in fluidized beds. Further investigations are left to future work.

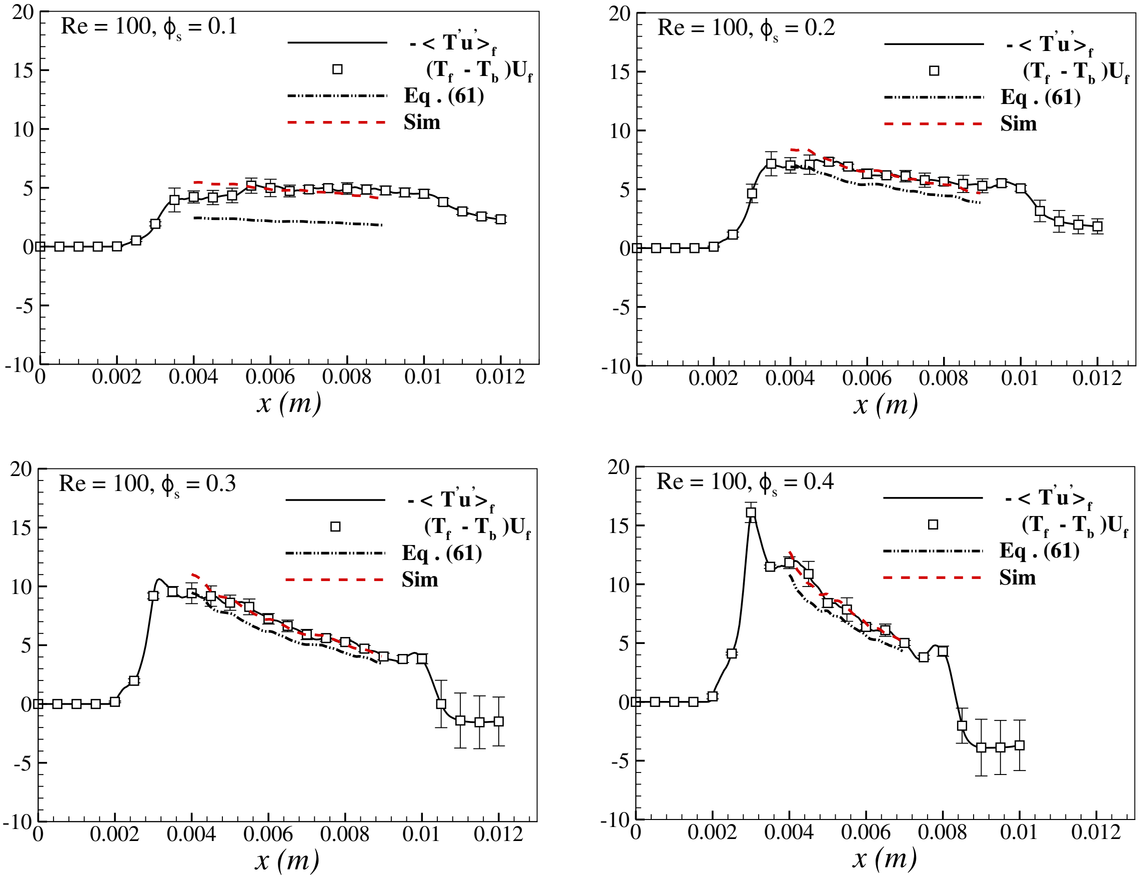

Fig. 23 Pseudo-turbulent heat flux. Same caption as in Fig. 21, at $Re = 100$

Acknowledgements This work was granted access to the HPC resources of CALMIP supercomputing center under the allocation P1529 and of CINES supercomputing center under the allocation A0022B10120. CALMIP and CINES are gratefully acknowledged. The authors wish to thank Ing. Pierre Elyakime for his support with the numerical code.

References

1. Wakao, N., Kaguei, S., Funazkri, T.: Effect of fluid dispersion coefficients on particle-to-fluid heat transfer coefficients in packed beds: correlation of Nusselt numbers. Chem. Eng. Sci. **34**(3), 325 (1979)
2. Gunn, D.J.: Transfer of heat or mass to particles in fixed and fluidised beds. Int. J. Heat Mass Transf. **21**(4), 467 (1978)
3. Feng, Z.G., Michaelides, E.E.: Heat transfer in particulate flows with Direct Numerical Simulation (DNS). Int. J. Heat Mass Transf. **52**(3), 777 (2009)
4. Deen, N.G., Kriebitzsch, S.H.L., van der Hoef, M.A., Kuipers, J.A.M.: Direct numerical simulation of flow and heat transfer in dense fluid-particle systems. Chem. Eng. Sci. **81**, 329 (2012)
5. Feng, Z.G., Musong, S.G.: Direct numerical simulation of heat and mass transfer of spheres in a fluidized bed. Powder Technol. **262**, 62 (2014)
6. Tavassoli, H., Kriebitzsch, S.H.L., van der Hoef, M.A., Peters, E.A.J.F., Kuipers, J.A.M.: Direct numerical simulation of particulate flow with heat transfer. Int. J. Multiph. Flow **57**, 29 (2013)
7. Uhlmann, M.: An immersed boundary method with direct forcing for the simulation of particulate flows. J. Comput. Phys. **209**(2), 448 (2005)
8. Deen, N.G., Peters, E.A.J.F., Padding, J.T., Kuipers, J.A.M.: Review of direct numerical simulation of fluid-particle mass, momentum and heat transfer in dense gas-solid flows. Chem. Eng. Sci. **116**, 710 (2014)
9. Tenneti, S., Sun, B., Garg, R., Subramaniam, S.: Role of fluid heating in dense gas-solid flow as revealed by particle-resolved direct numerical simulation. Int. J. Heat Mass Transf. **58**(1), 471 (2013)
10. Sun, B., Tenneti, S., Subramaniam, S.: Modeling average gas-solid heat transfer using particle-resolved direct numerical simulation. Int. J. Heat Mass Transf. **86**, 898 (2015)
11. Kruggel-Emden, H., Kravets, B., Suryanarayana, M.K., Jasevicius, R.: Direct numerical simulation of coupled fluid flow and heat transfer for single particles and particle packings by a LBM-approach. Powder Technol. **294**, 236 (2016)

12. Tavassoli, H., Peters, E.A.J.F., Kuipers, J.A.M.: Direct numerical simulation of fluid-particle heat transfer in fixed random arrays of non-spherical particles. Chem. Eng. Sci. **129**, 42 (2015)
13. Municchi, F., Radl, S.: Consistent closures for Euler–Lagrange models of bi-disperse gas-particle suspensions derived from particle-resolved direct numerical simulations. Int. J. Heat Mass Transf. **111**, 171 (2017)
14. Wang, Y., Sierakowski, A.J., Prosperetti, A.: Fully-resolved simulation of particulate flows with particles-fluid heat transfer. J. Comput. Phys. **350**, 638 (2017)
15. Vincent, S., Brändle de Motta, J.C., Sarthou, A., Estivalezes, J.L., Simonin, O., Climent, E.: A Lagrangian VOF tensorial penalty method for the DNS of resolved particle-laden flows. J. Comput. Phys. **256**, 582 (2014)
16. Ritz, J.B., Caltagirone, J.P.: A numerical continuous model for the hydrodynamics of fluid particle systems. Int. J. Numer. Methods Fluids **30**(8), 1067 (1999)
17. Kataoka, I.: Local instant formulation of two-phase flow. Int. J. Multiph. Flow **12**(5), 745 (1986)
18. Caltagirone, J.P., Vincent, S.: Sur une méthode de pénalisation tensorielle pour la résolution des équations de Navier-Stokes. Comptes Rendus de l'Académie des Sciences - Series IIB - Mechanics **329**(8), 607 (2001)
19. Fortin, M., Glowinski, R.: Méthodes de lagrangien augmenté: applications à la résolution numérique de problèmes aux limites. Méthodes mathématiques de l'informatique (Dunod, 1982)
20. Vincent, S., Caltagirone, J.P., Lubin, P., Randrianarivelo, T.N.: An adaptative augmented Lagrangian method for three-dimensional multimaterial flows. Comput. Fluids **33**(10), 1273 (2004)
21. Vincent, S., Sarthou, A., Caltagirone, J.P., Sonilhac, F., Février, P., Mignot, C., Pianet, G.: Augmented Lagrangian and penalty methods for the simulation of two-phase flows interacting with moving solids. Application to hydroplaning flows interacting with real tire tread patterns. J. Comput. Phys. **230**(4), 956 (2011)
22. Brändle de Motta, J.C., Breugem, W.P., Gazanion, B., Estivalezes, J.L., Vincent, S., Climent, E.: Numerical modelling of finite-size particle collisions in a viscous fluid. Phys. Fluids **25**(8), 083302 (2013)
23. Khadra, K., Angot, P., Parneix, S., Caltagirone, J.P.: Fictitious domain approach for numerical modelling of Navier–Stokes equations. Int. J. Numer. Methods Fluids **34**(8), 651 (2000)
24. Sarthou, A., Vincent, S., Caltagirone, J.P.: A second-order curvilinear to Cartesian transformation of immersed interfaces and boundaries. Application to fictitious domains and multiphase flows. Comput. Fluids **46**(1), 422 (2011)
25. Kramers, H.: Heat transfer from spheres to flowing media. Physica **12**(2), 61 (1946)
26. Ranz, W.E., Marshall, W.R.: Evaporation from drops: part II. Chem. Eng. Progress **48**(4), 173 (1952)
27. Whitaker, S.: Forced convection heat transfer correlations for flow in pipes, past flat plates, single cylinders, single spheres, and for flow in packed beds and tube bundles. AIChE J. **18**(2), 361 (1972)
28. Feng, Z.G., Michaelides, E.E.: A numerical study on the transient heat transfer from a sphere at high Reynolds and Peclet numbers. Int. J. Heat Mass Transf. **43**(2), 219 (2000)
29. Whitaker, S.: Diffusion and dispersion in porous media. AIChE J. **13**(3), 420 (1967)
30. Quintard, M., Whitaker, S.: Transport in ordered and disordered porous media: volume-averaged equations, closure problems, and comparison with experiment. Chem. Eng. Sci. **48**(14), 2537 (1993)
31. Vermorel, O., Bédat, B., Simonin, O., Poinsot, T.: Numerical study and modelling of turbulence modulation in a particle laden slab flow. J. Turbul. **4**, N25 (2003)
32. Levec, J., Carbonell, R.G.: Longitudinal and lateral thermal dispersion in packed beds. Part I: theory. AIChE J. **31**(4), 581 (1985)
33. Quintard, M., Kaviany, M., Whitaker, S.: Two-medium treatment of heat transfer in porous media: numerical results for effective properties. Adv. Water Resour. **20**(2), 77 (1997)
34. Sun, B., Tenneti, S., Subramaniam, S., Koch, D.L.: Pseudo-turbulent heat flux and average gas-phase conduction during gas–solid heat transfer: flow past random fixed particle assemblies. J. Fluid Mech. **798**, 299 (2016)
35. Buist, K.A., Backx, B.J.G.H., Deen, N.G., Kuipers, J.A.M.: A combined experimental and simulation study of fluid-particle heat transfer in dense arrays of stationary particles. Chem. Eng. Sci. **169**, 310 (2017)
36. Hamidouche, Z., Masi, E., Fede, P., Ansart, R., Neau, H., Hemati, M., Simonin, O.: In: Parente, A., De Wilde, J. (ed.,) Bridging Scales in Modelling and Simulation of Non-Reacting and Reacting Flows. Part I, Advances in Chemical Engineering, vol. 52, Academic Press, pp. 51–124 (2018)